Robust Bottom-Up Gold Filling of Deep Trenches and Gratings

D. Josell[1,*], W. Osborn[2], M.E. Williams[1], H. Miao[3],

[1] Materials Science and Engineering Division, National Institute of Standards and Technology, Gaithersburg, Maryland 20899, USA

[2] Materials Measurement Science Division, National Institute of Standards and Technology, Gaithersburg, Maryland, 20899, USA

[3] General Optics, LLC, Zionsville, IN 46077

Keywords: Electroplating, Gold, Gratings, Superconformal

ABSTRACT

This work extends an extreme variant of superconformal Au electrodeposition to deeper device architectures while exploring factors that constrain its function and the robustness of void-free processing. The unconventional bottom-up process is used to fill diffraction gratings with trenches 94 μm deep and 305 μm deep, with aspect ratios (height/width) of just below 20 and 15, respectively, in near-neutral 0.16 mol·L^{-1} $Na_3Au(SO_3)_2$ + 0.64 mol·L^{-1} Na_2SO_3 electrolyte containing 50 μmol·L^{-1} Bi^{3+}. Although the aspect ratios are modest compared to previously demonstrated void-free filling beyond AR = 60, the deepest trenches filled exceed those in previous work by 100 μm — a nearly 50 % increase in depth. Processes that substantially accelerate the start of bottom-up deposition demonstrate a linkage between transport and void-free filling. Final profiles are highly uniform across 65 mm square gratings because of self-passivation inherent in the process. Electron microscopy and electron backscatter diffraction confirm the fully dense Au and void-free filling suggested by the electrochemical measurements. X-ray transmission "fringe visibility" average more than 80 % at 50 kV X-ray tube voltage across the deeper gratings

and 70 % at 40 kV across the shallower gratings, also consistent with uniformly dense, void-free fill across the gratings.

INTRODUCTION

This work extends previous studies related to an unconventional bottom-up gold filling electrodeposition process[1-6] to deeper device architectures while exploring process robustness and the constraint of transport on its function. Fully dense Au filling of recessed trenches and vias on metallized patterned substrates followed by self-termination of the growth process without significant deposition, or overburden, on the overlying field is achieved. The high electron density of gold makes the deposits especially well-suited for use as X-ray absorbing material in gratings etched in silicon substrates.[7] Such gratings are essential for X-ray interferometry and phase-contrast imaging in both one-dimensional[8] (1D) and two-dimensional (2D) implementations[9], including in wave front sensing[7], highly accurate measurements of the phase gradient of illumination wavefronts[10] and the characterization and alignment of optics and focus of X-ray free-electron lasers[11,12] that themselves enable a wide range of dynamical studies of atoms, molecules, clusters, and materials in the physical and life sciences.

X-ray phase contrast imaging[13] has found widespread use in applications including biomedicine, material science and security. For biomedical applications in particular[14] it enables imaging of lower density materials such as tissue in conjunction with lower X-ray dose. However, imaging of the human torso requires gratings appropriate for hard X-rays; 70 kV and 120 kV X-ray tube voltages are representative of values used in grating-based thoracic studies[15,16], the values spanning the range used for conventional radiography of the skeleton and lungs[17]. Further, gratings with uniform metal filling across large areas would eliminate the difficult challenge associated

with stitching together smaller gratings for increased field of view as done in recent chest imaging[15-17] and mammography[18] and full body cadaver[19] studies.

Previous papers have addressed use of the bottom-up Au filling approach for fabrication of dense Au gratings having high aspect ratio features (AR, depth/width), with values exceeding 60, at micrometer scale pitch for applications requiring high spatial resolution and contrast. This work explores the bottom-up Au filling of gratings with trenches that are of somewhat larger pitch and more moderate aspect ratio. However, at more than 300 μm deep, they are appropriate for medical imaging of the human body and deeper than any filled before. The 65 mm gratings are patterned on 100 mm Si wafers although the process is fully compatible with scale-up to 200 mm, and potentially 300 mm or even 450 mm, diameter workpieces. The bottom-up gold deposition process allows void-free filling of complex architectures that are not achievable even with highly conformal deposition, e.g., of Au[20] or Ir[21]. It also serves as a more uniformly filling alternative to through-mask plating processes and architectures that require construction and use of a common back plane and nonconducting sidewalls[22,23].

Without additives, the $Na_3Au(SO_3)_2$ + Na_2SO_3 electrolyte yields slow and nominally uniform, i.e., conformal, deposition on all surfaces. The deposition reaction is inhibited by adsorption of sulfite and related Au complexes on the electrode surface. In contrast to the well detailed use of additives such as Tl^+ and pulse plating to improve the uniformity and smoothness of the Au deposits[24-28], the Bi^{3+} additive used here provides non-linear acceleration and bottom-up feature filling that have only begun to be detailed in the last several years. The behavior is entirely distinct from that detailed in other additive-derived superconformal[29-34] and bottom-up filling[35-39] processes, including those for Au[32-34,38,39]. Four important feature filling characteristics of the Bi^{3+}-derived filling are: 1) an extended but finite “incubation period” of conformal deposition, 2)

subsequent activation of deposition localized to the most recessed (i.e., bottom) surface of features, 3) continuing accelerated deposition with propagation yielding void-free filling and 4) self-passivation of the active growth front at a distance from the feature opening defined by operating conditions. The duration and detailed evolution of these four stages are impacted by electrolyte concentrations and pH, applied potential (and/or current), feature dimensions and convective transport conditions. Correlations between process parameters, electroanalytical response and feature filling behavior have been established[1-6] for electrolytes including x mol·L^{-1} $Na_3Au(SO_3)_2$ + 0.64 mol·L^{-1} Na_2SO_3, for x:[0.08, 0.16 and 0.32], of pH 8.5 to 10.5, with Bi^{3+} concentrations ranging from 1 μmol·L^{-1} to 50 μmol·L^{-1}. Void-free, bottom-up filling has been demonstrated in 1D arrays of trenches ranging from as shallow as 3 μm to as deep as 210 μm with aspect ratio from as low as 1.5 to more than 60. Trench widths have been nominally one-half their pitch in these arrays. Void-free, bottom-up filling has also been demonstrated in 2D arrays of vias 23 μm deep with AR = 23.[6]

The sustained passivation of deposition that occurs on the field and sidewalls of recessed features allows void-free filling through the highly active deposition that, following the incubation period, concurrently develops on the most recessed surface. A non-monotonic dependence of the passivation of the field on hydrodynamics, with faster flow sustaining the field in a passive state for a longer period of time, suggests the importance of the more quiescent environment and, perhaps, slowly developing gradients within filling features. In light of the known increase in the rates of both Au deposition and Bi adsorption with modest increase in alkalinity, perturbation of pH, possibly associated with SO_3^{2-} reduction, is a likely candidate for the localization of active deposition that underlies the bottom-up filling dynamic.

Deposition on the passive sidewalls is substantially slower than that on the active bottom

surface. However, in narrower and higher aspect ratio features the parabolic concentration profile associated with uniform passive deposition on the sidewalls can more readily dominate the linear gradient of metal ion concentration that is associated with active deposition on the bottom surface. Key-hole shaped voids observed upon failure to fill are clear indicators of the limitations on metal ion transport, at the very least as failure progresses. "Truncated bottom-up filling", where the start of bottom-up filling is followed by activation of a portion of the upper sidewalls prior to its completion, also manifests transport related keyhole shaped void formation, but it does so in conjunction with, and ultimately to the detriment of, bottom-up filling. While such gradients can be reduced by slower deposition, the use of lower overpotentials can increase the incubation period from minutes to days at the potentials required for void-free filling of especially deep features.

The shallower trenches used in this study, nominally 94 μm deep and 5.2 μm wide at 8 μm pitch, are deeper than the majority of features filled to date using these electrolytes. The deeper trenches, nominally 305 μm deep and nearly 21 μm wide at 32 μm pitch, are substantially deeper than any previously filled. The aspect ratios of these trenches, approaching 20 and 15, respectively, are fairly modest. Feature filling was accomplished in electrolyte of 0.16 $mol \cdot L^{-1}$ $Na_3Au(SO_3)_2$ with 0.64 $mol \cdot L^{-1}$ Na_2SO_3 as supporting electrolyte at pH of 9.0 and with 50 $\mu mol \cdot L^{-1}$ Bi^{3+} additive that has been the subject of electroanalytical analysis in the previous studies. Approaches for accelerated deposition, of practical significance given the multiday incubation periods experienced during filling of the deepest features, and process robustness are also examined, including the utility of the self-passivation for repair of improperly filled gratings. The Au filling is characterized at length scales from the micrometer scale of the Au microstructure and feature filling to the centimeter scale of filling uniformity across the gratings using scanning electron microscopy (SEM), X-ray transmission and Electron Backscatter Diffraction (EBSD).

GOLD DEPOSITION

Experimental Details

Silicon wafers 100 mm in diameter and 0.5 mm thick were patterned with square grating arrays 65 mm on a side. The trenches in the gratings are uninterrupted, i.e., without cross-bars for stabilization, but displacement (e.g., bowing) of the Si spacers in the Au-filled structures is observed to be minimal due to their absolute thicknesses and relatively low aspect ratios. A uniformly conductive seed layer for electrodeposition was formed by atomic layer deposition (ALD) of a Pt/Al_2O_3 bilayer (40 nm thick platinum on 10 nm thick Al_2O_3), ALD of Au not being possible, that provided continuous coverage on the scalloped sidewalls created by the Bosch process cycles. Previous studies have shown that, due to the bottom-up nature of filling, the scalloping does not impact filling. Exploratory filling experiments used sacrificial wafers that had been cleaved into fragments typically 3 mm wide by 12 mm long.

The bottom-up Au electrodeposition was conducted in 40 mL to 600 mL of electrolyte as convenient for the size of the specimen. The electrolytes included 0.32 $mol \cdot L^{-1}$ $Na_3Au(SO_3)_2$ (Technic Gold 25-F replenisher concentrate), diluted using 18 $M\Omega \cdot cm$ water, and 0.64 $mol \cdot L^{-1}$ Na_2SO_3. The pH of the electrolytes, in the range 9.7 to 9.8 as mixed, was adjusted down for use using H_2SO_4 diluted in distilled water sufficiently to avoid gold precipitation. The pH was adjusted up between deposits as required using NaOH dissolved in distilled water for greater control. The Bi^{3+} additive was introduced by anodic dissolution of 99.999 mass % Bi metal, the possibility of parasitic oxidative processes making stated concentrations upper bounds. Deposition on the rectangular wafer fragments was conducted with the specimen either rotating about one end from a Pt spindle, the patterned surfaces of the specimens facing either up or down and parallel to the

flow in the electrolyte (i.e., helicopter blade), or suspended and rotated about the longer vertical axis, as indicated. The suspended specimen geometry has a complicated flow field, but deposition can be limited to the patterned region of the substrate. The helicopter blade geometry provides better defined shear flow, but the slot in the spindle in which the substrates are clamped is immersed in the electrolyte with the specimen and also experiences Au deposition. Specimens were cross sectioned after deposition for characterization by SEM and EBSD using a process that has been detailed in the preceding studies. Full wafer deposition was accomplished with the wafer in a rotating disk electrode geometry using a system that has also been described previously. These gratings were characterized using X-ray interferometry.

Deposition was accompanied by acidification of the electrolyte, most likely associated with oxidation of sulfite to sulfate at the Pt anode, particularly during filling of larger substrates. The electrolyte pH was checked between specimens and adjusted accordingly. Potentials during deposition on planar as well as patterned substrates were measured relative to a Hg/Hg_2SO_4/saturated K_2SO_4 reference electrode (SSE). No attempt was made to compensate for potential drop across the electrolyte during deposition on the small rectangular specimens given deposition currents that were below 1 mA and system impedance measured to be $< 4\ \Omega$. Deposition on the full wafers, with current generally below 25 mA, was also uncompensated given the large active area and Pt sheet electrode of similar size.

Deposition in Trench Arrays

Deposition in this study used an electrolyte of 0.16 $mol \cdot L^{-1}$ $Na_3Au(SO_3)_2$ + 0.64 $mol \cdot L^{-1}$ Na_2SO_3 containing 50 $\mu mol \cdot L^{-1}$ Bi^{3+} that is nominally identical to that used to fill narrower and higher aspect ratio trenches. Filling in 94 μm deep 5.2 μm wide trenches at an 8 μm pitch is shown

as a function of applied potential in **Fig. 1**; it transitions from subconformal filling, to truncated bottom-up filling, to complete bottom-up filling as the deposition potential becomes less negative. A similar variation of Au filling with potential has been observed previously.

The current density transients associated filling of the 94 μm deep specimens in **Fig. 1** are shown in **Fig. 2a**. At all three potentials, initially low current density is followed by a rising transient that reflects nucleation and growth of Au on the Pt seed. At −0.76 V this transient takes approximately 11 h, the current stabilizing at approximately −0.7 $mA \cdot cm^{-2}$ once the specimen is entirely Au coated. The specimen sectioned toward the end of this plateau at 15 h exhibits only conformal Au from passive deposition. The rapid increase to approximately −1.4 $mA \cdot cm^{-2}$ that begins at approximately 16.5 h signals the start of bottom-up filling. The comparatively gradual increase that follows is consistent with relaxation of the gradient of metal ion concentrations as the distance to the active bottom surface is reduced by the bottom-up filling. However, its relatively modest scale (only ≈ 20 %), from about −1.5 $mA \cdot cm^{-2}$ to −1.9 $mA \cdot cm^{-2}$, as filling progresses up the height of the features suggests the deposition rate is controlled by potential-defined kinetics more than transport. The final decrease of current to just −0.3 $mA \cdot cm^{-2}$ that is nearly completed by 22 h reflects passivation of the deposits in the uniformly filled trenches imaged at 24 h. With deposition at −0.78 V the current density is still rising in the initial transient and the deposit remains conformal on the specimen sectioned at 9 h just before a second transient yielding even more rapid increase begins. Limited bottom-up filling at 15.2 h evidently commenced at the start of this second transient only to be truncated by the start of active deposition on the sidewalls. Deposition at −0.80 V is analogous but on an even shorter timescale; nucleation and growth of Au on the Pt layer is not yet even completed at 4 h when the already rapidly increasing current steepens its rate of ascent. Interestingly, the further acceleration of current density with the specimens that voided at −0.80 V

and −0.78 V occurs at current densities near the −1.4 mA·cm^{-2} value associated with early bottom-up filling at −0.76 V. In both cases the start of active deposition is evident, but with current densities rapidly in excess of −2.5 mA·cm^{-2}, portions of the sidewalls nearer the trench openings are included.

The charge density transients for the three specimens are shown in **Fig. 2b**. The charge density at the end of each transient, corresponding to self-passivation at -0.76 V and -0.78 V and emergence of deposition onto the field at -0.80 V, is larger at less negative potential. The value when filling is completed at -0.76 V is consistent with the filling observed in **Fig. 1**.

Filling of 305 μm deep 21 μm wide trenches at a 32 μm pitch in 0.16 mol·L^{-1} $Na_3Au(SO_3)_2$ + 0.64 mol·L^{-1} Na_2SO_3 electrolyte containing 50 μmol·L^{-1} Bi^{3+} is shown as a function of applied potential in **Fig. 3**. A vertical orientation of the specimens was used for improved control of the current associated with deposition. Because nucleation of Au on the Pt seed was problematic at the less negative potentials necessary for void-free filling of these deeper trenches a potentiodynamic process of 13 h at -0.76 V for nucleation and growth of the Au seed followed by a sequence of 5 mV steps, each of 2 h duration, to the filling potential was used. Deposition again transitions from subconformal, to truncated bottom-up, to void-free bottom-up filling at more positive values of the filling potential. The most negative potential at which void-free filling is observed, -0.72 V, is 40 mV positive of the -0.76 V potential at which void-free filling was obtained in the shallower trenches.

Current density and charge density transients associated with filling of the 305 μm deep specimens in **Fig. 3** are shown in **Fig. 4**. Variation between specimens during the first 21 h when the potential histories are identical is consistent with pH variation; nearly identical responses of the specimens filled at -0.72 V and -0.71 V reflect deposition in fresh electrolytes of slightly lower

pH ≈ 8.8 that were constituted and dosed with Bi^{3+} together. Despite this variation, it is evident that the incubation period before activation (of bottom and/or sidewalls) increases substantially as the deposition potential changes by only +25 mV across the four specimens. Although void-free filling is obtained for filling potentials of both -0.72 V and -0.71 V, only deposition at -0.71 V exhibits a gradually rising plateau after activation such as was observed with void-free filling of the shallower trenches at -0.76 V (**Fig. 2**). Once again, a modest fractional increase of current associated with the progress of bottom-up filling suggests limited impact of transport. Progressively higher maximum current densities are obtained with both voided and void-free specimens as the filling potential moves negative. The rapid increase of current upon activation at ≈ 65 h during filling at -0.72 V decelerates smoothly through both the maximum current density and the decline that marks the onset of self-passivation. The ≈ 40 % increase during the bottom-up filling from approximately -0.6 $mA \cdot cm^{-2}$ to nearly -0.85 $mA \cdot cm^{-2}$ suggests a more significant influence of transport that is consistent with faster deposition at the more negative potential. Filling potentials of -0.735 V and -0.73 V that yield truncated bottom-up filling also exhibit a clearly demarcated transition between the rise indicating activation across the substrate and a sloped plateau, the current density at this transition and the slope of the plateau both being higher at more negative potential. The transitions occur at current densities exceeding the highest value observed early in void-free filling at -0.72 V, i.e., approximately -0.6 $mA \cdot cm^{-2}$. As with the shallower trenches, the charge at completion increases substantially at less negative deposition potential, reaching values appropriate for complete filling after self-passivation at both -0.71 V and -0.72 V, consistent with the specimens in **Fig. 3**.

ACTIVE VERSUS PASSIVE DEPOSITION RATES

Visual comparison of the increase of current density upon activation of bottom-up filling to the passive current density preceding it is deceptive. The passive current density reflects deposition across the field, sidewalls and bottom of the patterned trenches. Accounting for the depth *d*, width *w* and pitch *P* of the trenches, this area is increased beyond that of the planar area by a multiple of $1 + 2\,d/P$ that is unchanged by conformal deposition. Dividing by the ≈ 25× larger surface area of the 94 μm deep 5.2 μm wide trenches at their 8 μm pitch, the pre-activation current density of -0.7 mA·cm^{-2} at -0.76 V in **Fig. 2a** corresponds to a passive deposition rate below -0.03 mA·cm^{-2}. In contrast, the incremental increase of current density from bottom-up filling reflects deposition only at the trench bottoms, an initial fraction w/P of the planar area that is reduced further by passive deposition on the sidewalls during the incubation period. Dividing by the area of the trench bottoms in the original pattern, the -0.7 mA·cm^{-2} increment upon activation of bottom-up filling suggests an active deposition rate of -1.1 mA·cm^{-2}; accounting for narrowing of the unfilled width by nearly 40 % during the incubation period, i.e., 20 C·cm^{-2} deposited during the 17 h incubation period from the 53 C·cm^{-2} charge for void-free filling predicted and observed, the active deposition rate is actually closer to -1.7 mA·cm^{-2}. The active and passive deposition rates thus differ by approximately a factor of sixty.

Similar analysis for the 305 μm deep 21 μm wide trenches at 32 μm pitch that bottom-up filled at -0.71 V converts the -0.3 mA·cm^{2} passive current density prior to activation, accounting for the 20× larger surface area, to a passive deposition rate of approximately -0.015 mA·cm^{-2}. The -0.2 mA·cm^{-2} increment upon activation of bottom-up filling using the original dimensions of the pattern, suggests an active current density on the trench bottoms of -0.3 mA·cm^{-2}; accounting for narrowing of the unfilled width by ≈ 20 %, i.e., 40 C·cm^{-2} deposited during the 83 h incubation period from the 190 C·cm^{-2} charge for void-free filling predicted and observed, the active

deposition rate is actually closer to -0.4 mA·cm^{-2}. In this case the active and passive deposition rates differ by only a factor of twenty five.

Comparing the results across the shallower and deeper specimens, the passive rates of < -0.03 mA·cm^{-2} and -0.015 mA·cm^{-2} differ by somewhat less than a factor of two. A more substantial difference is observed between the active rates of approximately -1.7 mA·cm^{-2} and nearly -0.4 mA·cm^{-2} for the shallower and deeper specimens, which differ by approximately a factor of 4.5.

Because the 50 mV difference in the deposition potentials certainly plays some role in the difference of the active current densities, a cyclic voltammogram for the electrolyte is shown in **Fig. 5**. It is plotted on a logarithmic scale for improved comparison of current densities on the negative-going scan and the positive-going scan over the -0.85 V to -0.7 V potential range relevant to these experiments. The passive deposition rate is reflected in the negative-going initial scan; it is considered an upper bound given that parasitic contributions might be significant at the low current density. The active deposition rate is reflected in the positive-going return scan. The active trace exhibits current density that is transport limited at more negative potentials, with kinetic control at potentials in the range of the filling experiments evident in the Tafel dependence, $J = J_0 e^{\frac{-\propto FV}{RT}}$ $(= J_0 10^{\frac{-\propto FV log_{10}(e)}{RT}})$, that manifests in the linear dependence on potential in the logarithmic plot. Fit over this full range, a charge transfer coefficient of $\alpha = 0.46$ is obtained, with $\alpha = 0.48$ obtained from fitting over the range -0.8 V and -0.7 V, using Faraday's constant $F = 96{,}485$ C·mol^{-1}, gas constant $R = 8.314$ J·mol^{-1}·K^{-1} and temperature T = 293 K for the room temperature experiments. Unlimited by transport, the active and passive deposition rates differ by more than a factor of 100 across this potential range.

The relative impacts of transport on active deposition at the bottoms of the 94 μm deep trenches at -0.76 V and the 305 μm deep trenches at -0.71 V can be inferred from comparison of the active

current densities beyond that anticipated given the difference in deposition potential. Using the measured Tafel dependence, the kinetically defined current densities J_i are related by the potential differential ΔV through $\frac{J_0}{J_1} = e^{\frac{\propto F \Delta V}{RT}}$. Using the (larger) measured charge transfer coefficient of $\alpha = 0.484$ relevant to the less negative potential range of the experiments, the ΔV = 50 mV difference between the potentials is associated with a ratio of 2.61 between the active current densities at the two potentials. The ratio associated with the potential difference is well below the 4.5 ratio of the active deposition rates obtained from the deposition currents. The lower active current in the deeper trenches is consistent with greater impact of metal ion depletion in the deeper features.

Previous studies have observed potential dependent kinetics for both the active and the passive states in cyclic voltammetry and chronoamperometry using RDEs, and the role of transport has also been explored in electroanalytical measurements using RDEs. While potential dependence of the rate of passive deposition has been observed in the current density of the plateau that precedes bottom-up filling the above results are the most direct indication of the impact that metal ion transport has on the active deposition rate during bottom-up filling itself. The analysis presented here for active deposition in bottom-up filling reflects the challenge of comparing deposition across feature dimensions where void-free filling necessitates different deposition potentials and spatially and temporally varying deposition rates are convolved with non-planar substrate geometry. Direct evaluation of active growth rates through measurement of fill height as a function of deposition time has been previously examined at significantly more negative potentials from -0.82 V to -0.90 V for different size features. In this work, as in that study, potentials for void-free filling change with feature depth, so that a common potential cannot generally be used for comparison of growth rates in features having substantially different dimensions.

ACCELERATING THE INCUBATION PERIOD

The use of modestly more negative potentials early in the deposition process to enable void-free filling with a shortened incubation period has been described previously; an initial potential -20 mV negative of that for void-free filling of 45 μm deep trenches reduced the incubation period from approximately 2 h to 1 h, and void-free fill was then achieved at the usual potential. A more aggressive process, the potential deviating -40 mV from conditions compatible with void-free filling, has just been detailed in **Fig. 4** for filling of the 305 μm deep trenches. However, the deviation in this case was limited to a period consistent with nucleation and coalescence of Au on the Pt seed layer, prior to activation of bottom-up deposition. Given that the incubation period was still three days long (!), further acceleration of bottom-up filling in these deep features is desirable.

Experiments were undertaken to determine whether the mechanism underlying bottom-up filling permitted substantially larger deviations from potentials yielding void-free deposition and the extension of such potentials even into activation of bottom-up filling itself. The experiments examined whether aggressive potentials could be maintained as long as the current density remained below values consistent with void-free bottom-up filling. A three step process was used: 1) potentiostatic control was used to maintain deposition at substantially more negative potential than appropriate for void-free filling; 2) when the rising current density reached a predetermined value potentiodynamic control was applied to maintain the current density at that value; 3) when the positive-trending potential reached the bottom-up filling potential of -0.72 V, potentiostatic control was reapplied to maintain it. Given the need for a meaningful relationship between the controlled (measured) current and the current density related to feature filling, particularly during the period of potentiodynamic control, the specimens were suspended in the electrolyte with the specimen holder outside the electrolyte to yield better defined areas of active deposition.

Use of a starting potential of -0.82 V and specimen rotation rate of 100 rpm yielded a rapid current rise during the initial period of potentiostatic control and an equally rapid depolarization of the potential during the subsequent period of potentiodynamic control. Macroscopic deposits associated with active deposition along the edges of the substrate and, in some cases, on the field within the area of the pattern were the origin of both. A starting potential of -0.80 V and rotation rate of 200 rpm generally avoided active deposition at these locations so that these conditions were used instead; in light of earlier observations regarding the role of convection as well as potential in suppressing deposition on the field the difference is not surprising. Experimental current density and potential histories are shown in **Fig. 6**. It is noteworthy that initial current densities for specimens where the patterned region extended out of the electrolyte to the holder are more than two orders of magnitude higher than those for specimens where the patterned region was immersed fully within the electrolyte with un-patterned substrate (i.e., field) extending to the holder. The anomalously high current density with the former geometry arises from deposition that began rapidly in trenches covered by the capillary meniscus, rather than the area immersed in the bulk electrolyte; the entire duration of the former current density transients likely overstates the current density associated with filling in the immersed area, to a rough approximation, by this initial value. Transients for two specimens, one with relatively high current density and one with relatively low current density as compared to the -0.4 $mA \cdot cm^{-2}$ value for void-free bottom-up filling, are shown for each substrate geometry. With all four specimens, nucleation and growth of Au on the Pt seed followed by acceleration of the Au deposition that accompanies Bi adsorption is reflected in the rising current density during the initial potentiostatic hold, depolarization during the potentiodynamic hold and rising current density during the final potentiostatic hold. Although there is significant variation, likely due to the noted capillary deposition, the two specimens

activated using lower current densities transit more rapidly from the more negative potentials than the two specimens activated using the higher current densities (**Fig. 6b**).

The specimens associated with the transients in **Fig. 6** are seen in **Fig. 7**. The trenches are slightly narrower toward the top so a superconformal process is necessarily required for void-free filling. Specimens 3 and 4, which were activated using current densities well below the -0.4 $mA \cdot cm^{-2}$ value of void-free filling at -0.72 V (**Fig. 4**), exhibit minimal deposition on the sidewalls near the trench openings and thin, uniform deposition on the sidewalls farther down. They also exhibit bottom-up deposition that indicates void-free filling would have been obtained with more time at the -0.72 V filling potential. In contrast, Specimens 1 and 2 exhibit a non-monotonic variation of thickness down the sidewalls and subconformal deposition, with deposit thickness increasing significantly from the bottom toward the top. Specimen 1, which was activated using a current density close to -0.5 $mA \cdot cm^{-2}$, exhibits imminent void formation. Specimen 2, which was activated at a current density closer to -0.4 $mA \cdot cm^{-2}$, exhibits a more modest inversion. Given the aspect ratios of features that have been previously filled, it is probable that void-free filling would still have been obtained upon continued deposition at -0.72 V in the latter case. Permitting deposition to accelerate to the range of -0.4 $mA \cdot cm^{-2}$ and beyond at -0.80 V evidently results in activation of deposition on both the upper sidewalls and the trench bottoms with significant metal ion depletion. The additional $\approx$ 2 h of accelerated Bi adsorption at -0.80 V experienced by Specimens 1 and 2 as compared to Specimens 3 and 4 (**Fig. 6b**) is clearly detrimental. The substantially higher active deposition rate at -0.80 V, 4.6× that at -0.72 V absent metal ion depletion according to the voltammetry in **Fig. 5**, likely plays a role as well.

Considered more broadly, activation and sustainable bottom-up filling have been achieved in at least two, and possibly three, of four specimens in approximately one day, only one-third the

incubation period in **Fig. 4**. Accelerated void-free filling is clearly possible if the limits of transport are accommodated. Perhaps no less significantly, these results suggest that transport limitations also underlie the previously noted need for less negative potentials in void-free filling of taller and narrower trenches.

PROCESS ROBUSTNESS

With void-free filling as defined by sidewall activation evidently limited only by metal ion transport, a wide variety of process control conditions and approaches should be compatible with the bottom-up Au filling dynamic. The process used to fill one full wafer grating is shown with an image of the filled grating in **Fig. 8**. In this case, a conservative rather than accelerated approach was used given the possibility of more substantial depletion at the wafer scale. Thus, the -0.76 V potential that yielded void-free filling for these shallower trenches in **Figs. 1** and **2** was applied initially but was stepped to the less negative potential of -0.745 V as the current increased with the activation of bottom-up filling. Typical of the bottom-up filling, once activated it accelerated even as the potential was stepped positive. Only upon the decrease of current indicating the onset of passivation was the potential stepped back to -0.76 V to bring the passivated surface closer to the field. Also typical, once self-passivation had begun deposition continued to decelerate even as the potential was stepped negative. The radial variation in reflectivity of the filled wafer results from a deposit that is essentially flush with the field toward the center of the wafer and ever so slightly recessed farther out.

As a matter of practical relevance, the robustness of the process for correction of errors in processing is also worthy of note. Even this self-passivating process can overshoot and deposit beyond feature openings if inappropriate conditions are used, in which case the surface deposits

can significantly reduce grating performance. However, an overfilled grating can be stripped (e.g., using aqua regia) either through a blanket etch or locally to reduce waste, until the remaining deposit lies beneath the field, and then the bottom-up filling process can be reapplied to the wafer with the conditions now corrected for self-passivation. An overfilled grating can thus be repaired quite readily. Such error and correction in filling are captured in **Fig. 9**. This wafer, with 305 μm deep trenches, was subjected to a sequence of three bottom-up filling processes. The initial bottom-up filling process was halted prematurely due to external factors. The second bottom-up filling process was used to complete filling but also deposited onto the field due to overly aggressive processing conditions. Etch back of the overdeposited Au was followed by a third process of bottom-up fill, with self-passivation yielding void-free filling flush to the field across the area of the grating. An interesting artifact of the localized etch and refill is variation of specular contrast between regions where the blanket etch left trenches filled to the field, so that bottom-up filling did not occur in the final process, and regions where additional localized etching left the deposit well below the field so that bottom-up filling did occur in the third process. Higher magnification images of two such regions, after a light blanket etch to remove Au from the field for contrast with the Pt coated Si between the trenches shows that the deposits are flush with the surface in both.

MICROSTRUCTURE

The nature of filling at the trench level having been captured through imaging by SEM, the distribution and orientation of grains in the void-free Au deposit were assessed by EBSD. Maps capturing the microstructure in the lower portion of one Au-filled trench, collected at 20 kV beam voltage and 2.5 nA beam current, are shown in **Fig. 10**. The grains are colored according to the family of crystalline planes whose normal is oriented along the direction indicated for the map:

normal to the substrate, normal to the sidewall and parallel to the trenches. Pixels that did not index during the mapping have been infilled only where all 8 nearest neighbors were indexed successfully; in such cases the infilled pixel was assigned the orientation of the neighboring pixel whose orientation was closest to the average orientation of the nearest neighbors. The maps are subdivided into 4 regions, and inverse pole figures (IPFs) below each indicate texture as a multiple of the fraction expected in a microstructure with randomly oriented grains.

The fine-grained layers immediately adjacent to the sidewalls are readily associated with conformal, passive deposition. The grains in these layers exhibit a strong (111) texture (purple) in the direction of the sidewall normal that, being perpendicular to the growth front, is also their growth direction. The associated IPFs show that the degree of texturing in the sidewalls is substantial, with the fraction of (111) oriented grains exceeding 7× that of a random distribution. A (111) growth texture was also noted in thin film deposits from a similar electrolyte[2]. Whether this texture is related to growth on the Pt seed layer or a general bias in the passive Au electrodeposition is unknown.

A “feathered” microstructure of elongated, columnar grains that are oriented inward and upward is seen in the central regions on either side of the midline of the trench. The increasingly vertical orientation of the elongated grains nearer the midline and their curvature nearer the sidewalls are consistent with upward propagation of the concave growth surface seen in the SEM micrographs. A similar microstructure was observed in bottom-up Au filled 210 μm deep trenches.[4] The two halves of the central regions exhibit no obvious texture in the maps or associated IPFs.

Orientation maps in substrate and pattern defined directions can be effective for assessing growth texture in deposits on perpendicular surfaces including the horizontal bottom surface and

vertical sidewalls of trenches and vias. However, the direction of the assessment must be adjusted to evaluate texture when growth is angled through filling that involves propagation of a profile with angled or curved surfaces.[40] Maps of the crystalline texture in directions spanning the full 180° range of in-plane orientations, the direction of assessment indicated by the incline angle (from the reference frame defined by the trench and substrate) and arrow above each, are shown in **Fig. 11**. The (111) growth texture (purple) of the deposits along the sidewalls is repeated for assessment directions inclined by 0° and, equivalently, 180°. There is also seen to be (111) growth texture in the left half of the central deposit in the map at 60° that aligns the direction of assessment with the axes of the elongated grains in that region; the same (111) texture is seen in the right half of the central deposit in the map at 120° that aligns the assessment with the axes of the grains. Indeed, the associated IPFs indicate that growth is biased toward (111) in the central region albeit less strongly than the deposits along the sidewall. The texture assessed by the IPF in these regions is impacted by the spatially varying inclination of the grains in the deposits as well as the heavy 60° <111> twinning that is visible upon closer inspection of the maps. Whether the texture and twinning are intrinsic to the bottom-up filling dynamic is not known.

Large, relatively equiaxed grains with (100) texture in the direction of the sidewall normal extending from the sidewalls to the midline observed closer to the trench opening are not shown. An analogous microstructure was previously noted along the upper sidewalls of the 210 μm deep Au filled trenches. Inconsistent with bottom-up filling as well as passive growth on the sidewalls, these grains reflect recrystallization that originates adjacent to the sidewalls.

FILL ASSESSMENT BY X-RAY FRINGE VISIBILITY MEASUREMENT

The quality and completeness of fill across the area of the gratings was determined by measurement of fringe visibility, a local property that can be quantitatively related to the amount of Au in the trenches, and thus the height and density of the Au deposits. The fringe visibility is mapped from a Moiré fringe pattern created by X-ray transmission through a pair of gratings. The experimental setup included an X-ray source, a tungsten slit placed approximately 3 cm downstream of the X-ray focal spot, the two gratings, approximately 60 cm away farther downstream and normal to the X-ray source with a small (0.35 cm for the 8-μm pitch grating pair and 0.41 cm for the 32-μm pitch grating pair) gap between them, and a phosphor screen read by a charge coupled device (CCD) camera through a focal lens serving as the detector several centimeters downstream of the gratings. This system is simpler than the imaging systems used in previous studies of bottom-up Au filled gratings and assessed regarding visibility for imaging. Values of visibility obtained for the imaging systems represent a composite picture of the measurement system as a whole;[41] the fringe visibilities obtained here for the paired gratings set an upper bound for the performance of imaging systems that incorporate them. Although not used here, systematic tilting of individual gratings under X-ray illumination can also provide information regarding geometries and filling.[42]

i. Experimental Determination of Fringe Visibility

With the two gratings aligned such that the trenches on each are parallel, the projection of the X-ray source through the trench array on grating 1(2) creates a pattern of intensity modulation on the phosphor screen due to the different attenuation experienced by X-rays traveling through the Au filled trenches versus the Si walls between them. These modulations are at a pitch $P_{1(2)}$ that is slightly larger than the pitch P of the trenches on the grating as defined by beam divergence and

distance from the detector but significantly below the resolution of the detector. Dilation of the pattern on the screen from each grating is determined by its distance from the screen, with $P_1 > P_2$ for grating 1 closer to the source. Their combination forms a beating pattern across the detector, i.e., a Moiré pattern; the distance between maxima in the pattern equals $P_1P_2/(P_1 - P_2)$. A schematic capturing the elements of the experimental geometry that underlie the Moiré pattern fringes is shown alongside experimental patterns obtained from transmission through two gratings with Au filled 94 μm deep 5.2 μm wide trenches at 8 μm pitch in **Fig. 12**. Minimum intensity regions of the fringes correspond to locations where the projected patterns from the two gratings are displaced one-half cycle so that the projection through the Si walls in one grating is centered over the projection through the Au-filled trenches in the other grating. Given the trench widths are 65 % of their pitch it can be understood that transmission is low because the X-rays must pass through at least one layer of highly attenuating Au across the entire area. The maximum intensity regions of the fringes, on the other hand, correspond to locations where the projecting patterns from the two gratings are in correspondence. In this case the overlapping Au filled trenches leave overlapping Si walls over 35 % of the area through which there is substantial X-ray transmission.

The approach thus permits both transmission minima and maxima to be measured in a single experiment. For assessment of grating quality alone this approach is an alternative to stepping one grating in its plane, through a distance of one trench spacing, to sequentially obtain maximum and minimum transmission conditions across the entire grating and detector in analogy to the process used for assessing the performance of imaging systems. As in such measurements, however, decreasing overall transmission toward the top and bottom edges of the grating is observed due to progressively greater angular misalignment of the trenches in the planar gratings and the divergent X-ray beam that occurs farther from the central axis of the system. This misalignment is usually

resolved in practice by bending the grating to match the geometry of the X-ray wavefront to improve transmission (although the present filling approach would permit filling of pre-bent wafers). Standard X-ray radiographs of absorption across the area of each grating (not shown) indicate uniform fill with the exception of a strip less than 2 mm wide along the edges of the 65 mm patterned regions at the ends of the trenches. Increased transmission through all four gratings in these narrow edge strips indicates reduced Au volume in the trenches due to either altered lithography or voided filling.

For transmitted X-ray intensity exhibiting a square wave dependence on position the fringe visibility might be evaluated from the difference of the local maximum and minimum intensities divided by their sum. However, the different pitches of the intensity patterns transmitted through the two gratings mean that the patterns are actually exactly in phase and exactly out of phase only over infinitesimally narrow regions. The intensity across the Moiré fringe is thus smoothly varying (see **Fig. 13**) and the fringe visibility is instead given by twice the amplitude of the first order Fourier component of the oscillation divided by the amplitude of the zeroth order Fourier component, $2\tilde{I}_1/\tilde{I}_0$.

The millimeter scale pitch of the experimental Moiré lines corresponds to the period marked on the right of the schematic. As configured, the 1.5 mm distance (specified on the detector screen) between adjacent Moiré fringes manifests the smoothed spatial variation of transmission through 177 trenches on the first 8 μm pitch grating and 178 trenches on the second. Not shown here, the 5.25 mm distance between the Moiré fringes obtained with the 32 μm pitch gratings manifests the smoothed spatial variation of transmission through 154 trenches on the first grating and 155 trenches on the second. The gratings in these experiments are oriented such that the trenches in both are nearly parallel to the x-direction, with an angular deviation $\theta < 1.5°$ between them. The

period of the modulation distance of the fringes in the y-direction is given by the interference distance associated with the beating as discussed above. If the trenches in the first grating are perfectly aligned with the *x* direction then the pitch of the intensity modulation in *x* is defined by the angular deviation θ between the trenches on the gratings and equals $P_2/\sin(\theta)$.

Fringe visibility maps across the grating pairs were obtained from the experimentally measured X-ray intensity maps at a number of X-ray tube voltages. The procedure is summarized in **Fig. 13**; the full details of the analysis can be found in Appendix A. Visibility maps were obtained at X-ray tube voltages of 40 kV and higher for the gratings with the shallower trenches and 50 kV and higher for those with the deeper trenches. An upper bound of 80 kV was defined by the limits of the power supply. Variation of surface finish across one of the deeper wafers, seen in **Fig. 9**, has no measurable impact on the values obtained, as expected. However, the values obtained are lower than the fringe visibilities actually associated with the transmitted X-rays because of the finite spatial resolution of the fluorescent screen used in the detector. Specifically, lateral bleeding of light within the phosphor screen smooths the spatial oscillation of luminous intensity associated with the Moiré fringes that are measured by the CCD camera as compared to the spatial oscillation of the X-ray intensity that induced the fringes. The result is a systematic reduction of the measured fringe visibility relative to that actually associated with X-ray transmission through the pairs of gratings. This point will be returned to in the modeling that follows.

ii. Modeling of Fringe Visibility

Prediction requires evaluation of X-ray transmission through the two gratings that underlies the oscillating intensity in the Moiré patterns detailed in **Fig. 12**. The fraction of X-rays that are transmitted through material of thickness *d* follows the relationship

$$T(d,E) = e^{-\mu_i(E)d}, \quad [1]$$

where $\mu_i(E)$ is the attenuation coefficient for material *i* and X-ray photon energy *E*. The attenuation coefficients for both Au and Si are plotted as a function of the X-ray photon energy in **Fig. 14a**. The substantial difference between absorption in Au and Si, a result of the very different electron densities in the materials, underlies the motivation for Au filling in Si gratings. Because the X-ray attenuation in both materials is also strongly influenced by the energy of the photons, accurate prediction of transmission also requires knowledge of the X-ray distribution. The X-ray spectrum $S(E)$ expected for each of the X-ray tube voltages used in the experimental study, normalized to a total flux of unity, is shown in **Fig. 14b**.

The fraction of X-rays of energy *E* transmitted through a pair of layers equals the product of the fractions transmitted through the separate layers,

$$T(d_1,E)T(d_2,E) = e^{-d_1\mu_{1(E)}}e^{-d_2\mu_2(E)}. \quad [2]$$

Given the significant energy dependence, transmission through such a bilayer is calculated by the discrete integral of transmission in 1 kV steps weighted by the appropriate X-ray spectrum for the X-ray tube voltage in **Fig. 14b**, i.e.,

$$T_{bilayer} = \sum_{E_{min}}^{E_{max}} S(E_i)T(d_1,E_i)T(d_2,E_i) = \sum_{E_{min}}^{E_{max}} S(E_i)e^{-d_1\mu_1(E)}e^{-d_2\mu_2(E)}. \quad [3]$$

Fringe visibility is modeled using a Fourier analysis of the periodic transmission through each grating, including the Au filled trenches and Si walls of the grating as well as the unetched thickness of the underlying 0.5 mm thick Si wafer, to determine the spatial variation of transmitted X-ray intensity across the detector. The model also accounts for lateral spreading of the light signal generated by absorption of the X-rays impinging on the phosphor screen that limits detector resolution. The model is detailed in Appendix B.

iii. Comparison of Experiment and Prediction

The experimental values of fringe visibility are compared to the values predicted for fully Au filled gratings in **Fig. 15**. The dense, uniform gold filling obtained at the more positive potentials in **Figs. 1** and **3** is manifest in the high, spatially uniform values of fringe visibility obtained with the gratings. The measured fringe visibilities agree very well with the predicted values for conditions where the full spectrum of X-rays generated at the X-ray tube voltage is well attenuated by the Au layer of a single grating, as is the case with the 305 μm grating pairs at the 50 kV and 60 kV X-ray tube voltages. The measured fringe visibilities exceed the predicted values when the Au layer of a single grating does not strongly attenuate the full spectrum because a significant fraction of the higher energy X-rays in these spectra transit the phosphor screen without being absorbed. Specifically, because these higher energy X-rays are associated with lower fringe visibility, the experimental bias toward lower energy photons results in measured values of fringe visibility that are higher than those actually associated with the full spectrum. Correction for this measurement error was not possible in the absence of information regarding the energy-dependent response of the phosphor screen.

SUMMARY AND CONCLUSIONS

Near neutral electrolytes containing $Na_3Au(SO_3)_2$ with accelerating 50 $\mu mol \cdot L^{-1}$ Bi^{3+} additive have been used to obtain void-free, bottom-up filling of deep and moderately high aspect features. These include the deepest trenches filled using this bottom-up Au filling process (and, to the knowledge of the authors, any other) to date. Analysis of current and deposition charge transients obtained during filling of the features provide further information regarding the impact of metal ion transport on the filling evolution. Specifically, the results suggest that conditions for which

passive and/or active deposition rates substantially approach the transport limit define the boundary between truncated bottom-up filling and void-free bottom-up filling. This is consistent with extension of the processing range for void-free filling to more negative potentials in experiments with electrolytes having higher concentrations of $Na_3Au(SO_3)_2$ as well as in shallower or wider trenches.

The uniformity of filling across wafer scale gratings was assessed through fringe visibility values from Moiré fringe patterns at X-ray tube operation voltages from 40 kV to 80 kV. High values of fringe visibility, consistent with dense, void-free filling of the structures, were obtained with little variation across all but the edges of the 6.5 cm square gratings. The values and uniformity of the fringe visibility make clear the potential of the bottom-up Au filled gratings for imaging of the human body, including assessment of pulmonary diseases. The filling approach is ideal given the need for large gratings with Au filled deep and moderately high aspect ratio features; indeed, it should also be possible to fill gratings that have been curved, minimizing the stresses required to accommodate divergence of the X-ray source. Straightforward extension of the filling approach to the larger 200 mm wafers, or even the 300 mm wafers that are the mainstream of commercial semiconductor processing, should enable ready application to full body imaging that has to date required scanning with smaller gratings or stitching of multiple gratings due to limitations of the processes used in their fabrication.

APPENDIX A: FRINGE VISIBILITY DETERMINATION

The intensity across the *x*-*y* area of the Moiré fringe pattern in the X-ray irradiated phosphor screen was measured on the CCD camera at a pixel size of 61.7 μm in *x* direction rows and *y* direction columns. The Fourier Transform of the data along the *y* direction column was obtained

at each position *x*. Given the discrete nature of the data, the Fourier Transform integral over the length of the pattern in the *y* direction at each of the ≈ 1099 positions x_m across the 67.8 mm width (on the screen) was accomplished using a sum over the *y*-position datapoints, i.e., a Fast Fourier Transform (FFT)

$$\tilde{I}(x_m, k_j) = \sum_{n=0}^{N} I(x_m, y_n) e^{-2\pi i k_j y_n} \quad [A1]$$

over the N ≈ 340 datapoints along the 21 mm length L. Permitted wavenumbers in the FFT are k_j = j/21 mm^{-1} with |j|: 0, 1, 2, 3… ≤ 1/(2*0.0617) mm^{-1} in accord with the span in the y direction and the pixel size. Strong 0th and ± 1st order, as well as weaker ± 2nd order, primary peaks reflecting the 1.5 mm fringe spacing in *y* can be seen in the amplitude $|\tilde{I}(x_o, k_j)|$ of the FFT at the particular location x_o along the *x* direction plotted against the wavenumber *k* in **Fig. 13**. A map is shown for the amplitude $|\tilde{I}(x, k_j)|$ of the fringe pattern across the 67.8 mm width. The amplitude is essentially unchanged across the width of the map. Locally defined values of the Fourier coefficients used to obtain the fringe visibility were obtained from the inverse Fourier transform of $\tilde{I}(x, k_j)$ with contributions limited to the corresponding 0th and 1st order peaks, i.e., evaluating

$$\tilde{I}_{0,1}(x_m, y_n) \propto \sum_{\Delta k_{0,1}} \tilde{I}(x_m, k_j) e^{2\pi i k_j y_n} \quad [A2]$$

around the relevant peak as shown by the indicated ranges of wavenumber. The range Δk_0, -0.5/1.5 mm^{-1} ≤ k_j ≤ 0.5/1.5 mm^{-1}, is used to calculate the zeroth order Fourier coefficient as a function of position while the range Δk_1, 0.5/1.5 mm^{-1} ≤ k_j ≤ 1.5/1.5 mm^{-1}, is used to calculate the first order Fourier coefficient as a function of position. The fringe visibility at location (x_m, y_n) was obtained from $2|\tilde{I}_1(x_m, y_n)|/|\tilde{I}_0(x_m, y_n)|$; values at the 61.7 μm pixel resolution of the original fringe pattern in *x* were obtained at locations y_n that are spaced by 1.4 mm, which is slightly smaller than $1/\Delta k_0$ = 1.5 mm, the fringe spacing in *y*, finer resolution being inappropriate. These values were averaged over 1.4 mm intervals of *x* to obtain an approximately square pixilation in the fringe

visibility map. For these gratings and this X-ray tube voltage the average fringe visibility across the 21.0 mm × 67.8 mm region is 0.711 with a standard deviation of ± 0.067. The phase of the fringe at location (x_m, y_n) was obtained from $atan(Im[\tilde{I}_1(x_m, y_n)], Re[\tilde{I}_1(x_m, y_n)])$; it cycles from left to right as the fringes translate in the *y* direction with increasing *x*.

The analyses for the 94 μm deep 8 μm pitch and 305 μm deep 32 μm pitch wafer pairs were conducted over areas whose lengths L in the Fourier transformed *y* direction was approximately an integer multiple of the respective period of the fringe spacing in the same direction in order to be consistent with periodic boundary conditions at the top and bottom of the intensity map. The vertical extent *L* was also limited to reduce the impact of decreasing intensity farther from the central axis caused by increasing misalignment of the grating and X-ray beam. Together, these prevent convolution of a higher frequency $sinc(2\pi kL)$ function onto the primary peaks in the FFT that causes artifactual oscillations in the fringe visibility maps.

APPENDIX B

Fringe visibility values are predicted for full Au filling in the gratings accounting for: 1) the full spectral solution of the Moiré interference pattern produced by transmission through the pair of gratings and 2) the impact of measurement resolution that reduces the amplitude of shorter period oscillations. Transmission of X-rays to the screen is quantified by evaluating transmission across the Au-filled gratings i:[1, 2] at pitch P_i on the screen using their symmetrical Fourier expansions

$$T_i(y) = \frac{a_0}{2} + \sum_{n=1}^{\infty} a_{in} cos\left(\frac{2n\pi y}{P_i}\right) \quad [B1]$$

where it has been assumed for convenience that the projection through the middle of one Au filled trench on each grating occurs at the origin $y = 0$. The coefficients a_{in} for the rectangular wave

profiles are determined by fitting the transmitted intensity $T_i(y)$ through the regions of Au filled trench over Si substrate, $T_{Au+sub}(y)$, and regions of Si wall over Si substrate, $T_{Si+sub}(y)$, to account for the grating and 0.5 mm thick Si wafer in which the grating is embedded. For convenience, the rectangular wave of transmitted intensity through the Au filled grating as well as the integrals involved in its Fourier decomposition are initially expressed in the pitch *P* of the grating that exists just after the X-ray beam passes through the grating, rather than in the pitch P_i of the transmitted intensity on the screen,

$$T_i(y) = T_{Au+sub}\ for\ y{:}\left[-\frac{P\beta}{2},\frac{P\beta}{2}\right]\ \ ;\ \ T_i(y) = T_{Si+sub}\ for\ y{:}\left[-\frac{P}{2},-\frac{P\beta}{2}\ ;\ \frac{P\beta}{2},\frac{P}{2}\right] \qquad [B2]$$

with duty cycle $\beta = w_{Au}/P = 0.65$ the areal fraction of Au across both sets of gratings. Because the experiments are conducted on two nominally identical, fully Au filled gratings the coefficients are the same for both wafers, i.e., $a_{1n} = a_{2n} \equiv a_n$ for all *n*. The coefficients are obtained from the rectangular wave profile by $T_i(y)$ using the Fourier decomposition formulas

$$a_0 = \frac{2}{P}\int_{-P/2}^{P/2} T_i(y)\,dy = 2T_{Au+sub} + 2(1-\beta)(T_{Si+sub} - T_{Au+sub}) \qquad [B3]$$

and

$$a_n = \frac{2}{P}\int_{-P/2}^{P/2} T_i(y)cos\left(\frac{2\pi ny}{P}\right)dy = 2(1-\beta)(T_{Si+sub} - T_{Au+sub})sinc[(1-\beta)n\pi] \qquad [B4]$$

The term in Eq. [B3] is twice the spatial average of the transmitted intensity. The coefficients of the oscillatory terms found in Eq. [B4] include a $sinc[(1-\beta)n\pi]$ dependence for more general rectangular, rather than square, wave ($\beta \neq 0.5$), i.e., trench width not equal to Si wall width. The intensity on the screen is given by the transmission through the pair of grating, which, as noted previously, is the product of transmission through each

$$T_1(y)T_2(y) = \left[\frac{a_0}{2} + \sum_{n=1}^{\infty}\left(a_n cos\left(\frac{2n\pi y}{P_1}\right)\right)\right]\left[\frac{a_0}{2} + \sum_{n=1}^{\infty}\left(a_n cos\left(\frac{2n\pi y}{P_2}\right)\right)\right] \qquad [B5]$$

with the pitch of each dilated at the screen appropriately and scaling of the transmitted intensities due to dilation ignored because only ratios of terms are used in the analysis. Consistent with the spatial resolution of the detector system, only the cross terms of the product associated with the uniform (average) intensity and the two longest wavelength harmonics from interference between the two pitches are kept

$$T_1(y)T_2(y) \approx \frac{{a_0}^2}{4} + \frac{{a_1}^2}{2} cos\left[\left(\frac{1}{P_1} - \frac{1}{P_2}\right) 2\pi y\right] + \frac{{a_2}^2}{2} cos\left[\left(\frac{1}{P_1} - \frac{1}{P_2}\right) 4\pi y\right] \quad \text{[B6]}$$

These three terms are the Fourier components observed in the transform intensity map in **Fig. 11**: the average intensity captured in the 0th order term, the intensity oscillation associated with the Moiré fringes defined by the 1st order longer wavelength harmonic, and the 2nd order harmonic. The fringe visibility is given by the 1st order coefficient ${a_1}^2/2$ divided by the 0th order coefficient ${a_0}^2/4$; the multiple of 2 is omitted because the coefficient of $cos[2\pi ky]$ is already 2× the coefficient of the complex exponential in Eq. [A2]. The coefficients are expressed in terms of the transmission through the Au and Si layers of both grating, their duty cycle and the underlying Si according to Eqs. [B3] and [B4]. Transmission according to Eq. [B6] is evaluated summing contributions across the X-ray spectrum in **Fig. 12b** appropriate to the X-ray tube voltage being modeled and using the X-ray attenuation behavior in **Fig. 12a** to evaluate the terms T_{Au+sub} and T_{Si+sub}.

Bleeding of light laterally across the phosphor screen that converts the transmitted X-rays to the optical wavelength photons recorded by the CCD camera spreads light from otherwise sharp signals. Signal variation across shorter distances is damped by a greater amount; there is no impact on uniform illumination. Reduction of the amplitude of the optical Moiré fringes relative to the oscillations in the original X-ray intensity, without impact on the average intensity, reduces the fringe visibility measured relative to the actual fringe visibility of the pair of gratings. Because the

light intensity measured on the CCD camera is the *convolution* of the optical signal generated by the X-ray intensity and the line spread function (*LSF*) that defines the one dimensional spreading of the light within the phosphor screen the transform of the measured Moiré fringe intensity distribution is the *product* of the transform of the illuminating X-ray intensity and the transform of the *LSF*. Evaluation of the experimental *LSF* and thereby its transform thus allows prediction of the fringe visibility from the transform of the X-ray intensity distribution predicted in Eq. [B6].

The edge spread function *ESF*(*y*), of which the *LSF*(*y*) is the derivative, was determined by placing the phosphor screen directly on the metallized grating and fitting the measured light intensity distribution resulting from X-ray transmission as a function of the distance *y* from the lithographically defined edge between the (65 % Au + 35 % Si) material of the 65 mm square grating and the pure Si wafer surrounding it; for enhanced accuracy the system geometry was modified to bring the spatial resolution in the camera to 9.46 μm per pixel. The derivative was fit with the symmetrical Lambert-Beer exponential decay $LSF(y) = e^{-a|y|}$ appropriate for absorption of light in proportion to intensity over a length scale $1/a$. Fits were obtained as a function of the distance from the edge after averaging the data along 50 pixel wide regions of the edge to improve the signal to noise ratio. An average value and standard deviation of a = 0.00780 $\pm$ 0.00060 μm^{-1} or, equivalently, $1/a = 128 \pm 11$ μm, were obtained from the data evaluated over 38 different regions. The full width half max of the associated exponentially decaying spread of illumination along an infinitesimally fine line is thus 179 ± 14 μm.

Scaling the 0th and 1st order coefficients in Eq. [B6] by the transform of the *LSF*

$$\widetilde{LSF}(k) = \frac{2a}{a^2+(2\pi k)^2} \qquad \text{[B7]}$$

evaluated at k = 0 and k = 1/(Moiré fringe spacing), respectively, yields the corrected result

$$Fringe\ Visibility = \mathbb{C}(k)\frac{2{a_1}^2}{{a_0}^2} \qquad \text{[B8]}$$

Where $\mathbb{C}(k) = \widetilde{LSF}(k)/\widetilde{LSF}(0) = \widetilde{LSF}(k)/2$ as expressed in Eq. [B7] accounts for the detector resolution at all values of X-ray tube voltage. The fringe visibility for the 8 μm grating is suppressed by $\mathbb{C}(1/0.929\ mm) = 0.57$. The fringe visibility for the 32 μm grating is suppressed by $\mathbb{C}(1/1.132\ \text{mm}) = 0.66$.

ACKNOWLEDGEMENTS

This work was performed in part at the University of Michigan Lurie Nanofabrication Facility. We acknowledge Dr. Jorge Barreda for fabrication assistance.

REFERENCES

1. D. Josell and T. P. Moffat, *J. Electrochem. Soc.*, **166**, D3022 (2019).

2. S. Ambrozik, T.P. Moffat, C. Zhang, H. Miao and D. Josell, *J. Electrochem. Soc.*, **166**, D443 (2019).

3. D. Josell, M. Williams, S. Ambrozik, C. Zhang and T.P. Moffat, *J. Electrochem. Soc.*, **166**, D487 (2019).

4. D. Josell, S. Ambrozik, M.E. Williams, A.E. Hollowell, C. Arrington, S. Muramoto and T.P. Moffat, *J. Electrochem. Soc.*, **166**, D898 (2019).

5. D. Josell, Z. Shi, K. Jefimovs, L. Romano, M. Stampanoni and T. P. Moffat, *J. Electrochem. Soc.*, **167**, 132504 (2020).

6. D. Josell, Z. Shi, K. Jefimovs, V. A. Guzenko, C. Beauchamp, L. Peer, M. Polikarpov and T. P. Moffat, *J. Electrochem. Soc.*, **168**, 082508 (2021).

7. S. Rutishauser, L. Samoylova, J. Krzywinski, O. Bunk, J. Grünert, H. Sinn, M. Cammarata, D. M. Fritz, and C. David, *Nat. Commun*., **3**, 947 (2012).

8. T. Weitkamp, A. Diaz, C. David, F. Pfeiffer, M. Stampanoni, P. Cloetens and E. Ziegler, *Opt. Express* **13**, 6296 (2005).

9. I. Zanette, T. Weitkamp, T. Donath, S. Rutishauser, and C. David, *Phys. Rev. Lett.*, **105**, 248102 (2010).

10. Y.W. Liu, M. Seaberg, D.L. Zhu, J. Krzywinski, F. Seiboth, C. Hardin, D. Cocco, A. Aquila, B. Nagler, H.J. Lee, S. Boutet, Y.P. Feng, Y.T. Ding, G. Marcus, and A. Sakdinawat, *Optica*, **5**, 967 (2018).

11. P. Emma, R. Akre, J. Arthur, R. Bionta, C Bostedt, J. Bozek, A. Brachmann, P. Bucksbaum, R. Coffee, F.J. Decker, Y. Ding, D. Dowell, S. Edstrom, A. Fisher, J. Frisch, S. Gilevich, J. Hastings, G. Hays, P. Hering, Z. Huang, R. Iverson, H. Loos, M. Messerschmidt, A. Mtahnahri, S. Moeller, H.D. Nuhn, G. Pile, D. Ratner, J. Rzepiela, D. Schultz, T. Smith, P. Stefan, H. Tompkins, J. Turner, J. Welch, W. White, J. Wu, G. Yocky and J. Galayda, *Nat. Photon*., **4**, 641 (2010).

12. C. Pellegrini, A. Marinelli, and S. Reiche, *Rev. Mod. Phys.*, **88**, 015006 (2016).

13. A. Snigirev, I. Snigireva, V. Kohn, S. Kuznetsov and I. Schelokov, *Rev. Sci. Instrum*., **66**, 5486 (1995).

14. J. Vila-Comamala, L. Romano, K. Jefimovs, H. Dejea, A. Bonnin, A. C. Cook, I. Planinc, M. Cikes, Z. Wang, and M. Stampanoni, *Opt. Express*, **29**, 2049 (2021).

15. F.T. Gassert, T. Urban, M. Frank, K. Willer, W. Noichl, P. Buchberger, R. Schick, T. Koehler, J. von Berg, A.A. Fingerle, A.P. Sauter, M.R. Makowski, D. Pfeiffer and F. Pfeiffer, *Radiology*, **301**, 389 (2021).

16. K. Willer, A.A. Fingerle, W. Noichl, F. De Marco, M. Frank, T. Urban, R. Schick, A. Gustschin, B. Gleich, J. Herzen, T. Koehler, A. Yaroshenko, T. Pralow, G.S. Zimmermann, B.

Renger, A.P. Sauter, D. Pfeiffer, M.R. Makowski, E.J. Rummeny, P.A. Grenier and F. Pfeiffer, *L. Digit. Health*, **3**, e733 (2021).

17. A.P. Sauter, J. Andrejewski, F. De Marco, K. Willer, L.B. Gromann, W. Noichl, F. Kriner, F. Fischer, C. Braun, T. Koehler, F. Meurer, A.A. Fingerle, D. Pfeiffer, E. Rummeny, J. Herzen, and F. Pfeiffer, *Scientific Reports*, **9**, 8699 (2019).

18. C. Arboleda, Z.T. Wang, K. Jefimovs, T. Koehler, U. Van Stevendaal, N. Kuhn, B. David, S. Prevrhal, K. Lang, S. Forte, R.A. Kubik-Huch, C. Leo, G. Singer, M. Marcon, A. Boss, E. Roessl and M. Stampanoni, *European Radiology*, **30**, 1419 (2020).

19. J. Andrejewski, F. de Marco, K. Willer, W. Noichl, A. Gustschin, T. Koehler, P. Meyer, F. Kriner, F. Fischer, C. Braun, A.A. Fingerle, J. Herzen, F. Pfeiffer and D. Pfeiffer, *European Radiology Experimental*, **5**, 6 (2021).

20. K. Jefimovs, J. Vila-Comamala, C. Arboleda, Z. Wang, L. Romano, Z. Shi, M. Kagias, M. Stampanoni, *Micromachines*, **12**, 517 (2021).

21. J. Vila-Comamala, L. Romano, V. Guzenko, M. Kagias, M Stampanoni and K. Jefimovs, *Microelectron. Engin.*, **192**, 19 (2018).

22. L. Romano, J. Vila-Comamala, K. Jefimovs, and M. Stampanoni, *Advan. Engin. Mater.*, **22**, 2000258 (2020).

23. M. Kagias, Z.T. Wang, V.A. Guzenko, C. David, M. Stampanoni and K. Jefimovs, *Materials Science in Semiconductor Processing*, **92**, 73 (2019).

24. H. Honma and Y. Kagaya, *J. Electrochem. Soc.*, **140**, L135 (1993).

25. T. Osaka, A. Kodera, T. Misato, T. Homma and Y. Okinaka, *J. Electrochem. Soc.*, **144**, 3462 (1997).

26. Y. Okinaka and M. Hoshino, *Gold Bulletin* **31**, 3 (1998).

27. T.A. Green and S. Roy, *J. Electrochem. Soc.*, **153**, C157 (2006).

28. T. A. Green, *Gold Bulletin*, **40**, 105 (2007).

29. T.P. Moffat, D. Wheeler, W.H. Huber, and D. Josell, *Electrochem. Solid-State Lett*., **4**, C26 (2001).

30. Josell, D. Wheeler, W.H. Huber, J.E. Bonevich and T.P. Moffat, *J. Electrochem. Soc.*, **148**, C767 (2001).

31. D. Wheeler, D. Josell and T.P. Moffat, *J. Electrochem. Soc.*, **150**, C302 (2003).

32. Josell, C.R. Beauchamp, D.R. Kelley, C.A. Witt and T.P. Moffat, *Electrochem. Solid-State Lett.* **8**, C54 (2005).

33. D. Josell, D. Wheeler and T.P. Moffat, *J. Electrochem. Soc.*, **153**, C11 (2006).

34. D. Josell and T.P. Moffat, *J. Electrochem. Soc.*, **160**, D3009 (2013).

35. T.P. Moffat and D. Josell, *J. Electrochem. Soc.*, **159**, D208 (2012).

36. D. Josell, D. Wheeler and T.P. Moffat, *J. Electrochem. Soc.*, **159**, D570 (2012).

37. D. Wheeler, D. Josell and T.P. Moffat, *J. Electrochem. Soc.*, **160**, D3260 (2013).

38. D. Josell and T.P. Moffat, *J. Electrochem. Soc.*, **160**, D3035 (2013).

39. D. Josell and T.P. Moffat, *J. Electrochem. Soc.*, **164**, D327 (2017).

40. S.-H. Kim, H.-J. Lee, T.M. Braun, T.P. Moffat and D. Josell, *J. Electrochem. Soc.*, **168**, 112501 (2001).

41. T. Thuering and M. Stampanoni, *Phil. Trans. R. Soc. A*, **372**, 20130027 (2014).

42. N. Gustschin, A. Gustschin, P. Meyer, M. Viermetz, P. Riederer, J. Herzen, J. Mohr and F. Pfeiffer, *Optics Express*, **27**, 15943 (2019).

43. https://physics.nist.gov/PhysRefData/XrayMassCoef/ElemTab/z79.html

44. J.M. Boone and J.A. Seibert, *Med. Phys.*, **24**, 1661 (1997).

FIGURES

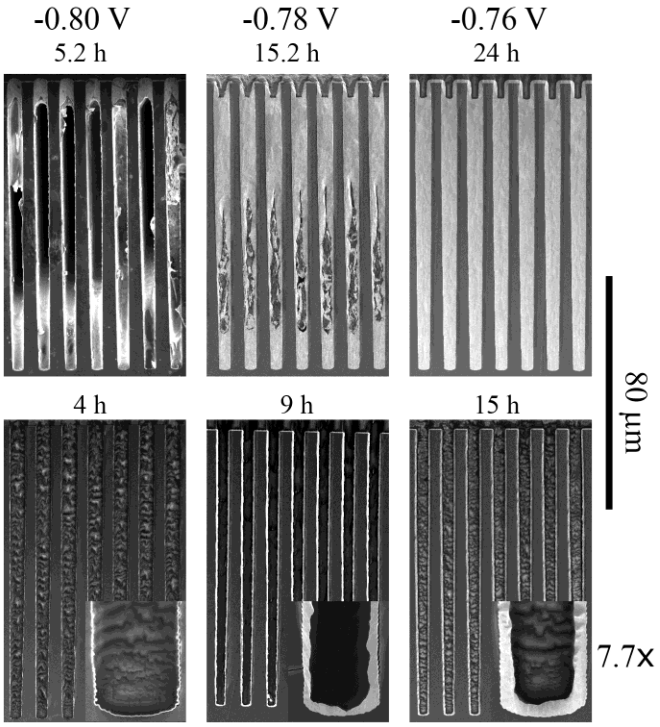

Figure 1: Scanning electron microscope images of Au electrodeposits after deposition at the indicated potentials in cross-sectioned gratings with 94 μm deep 5.2 μm wide trenches at 8 μm pitch; epoxy and polishing debris are visible in the unfilled regions. Filling is shown for two times at each potential. Higher magnification images capturing deposit thickness at the bottom of the partially filled trenches are inset. All rotating at 200 rpm (400π rad·min^{-1}) with flow parallel to the field in 0.16 mol·L^{-1} $Na_3Au(SO_3)_2$ + 0.64 mol·L^{-1} Na_2SO_3 electrolyte of pH 9.0 containing 50 μmol·L^{-1} Bi^{3+}.

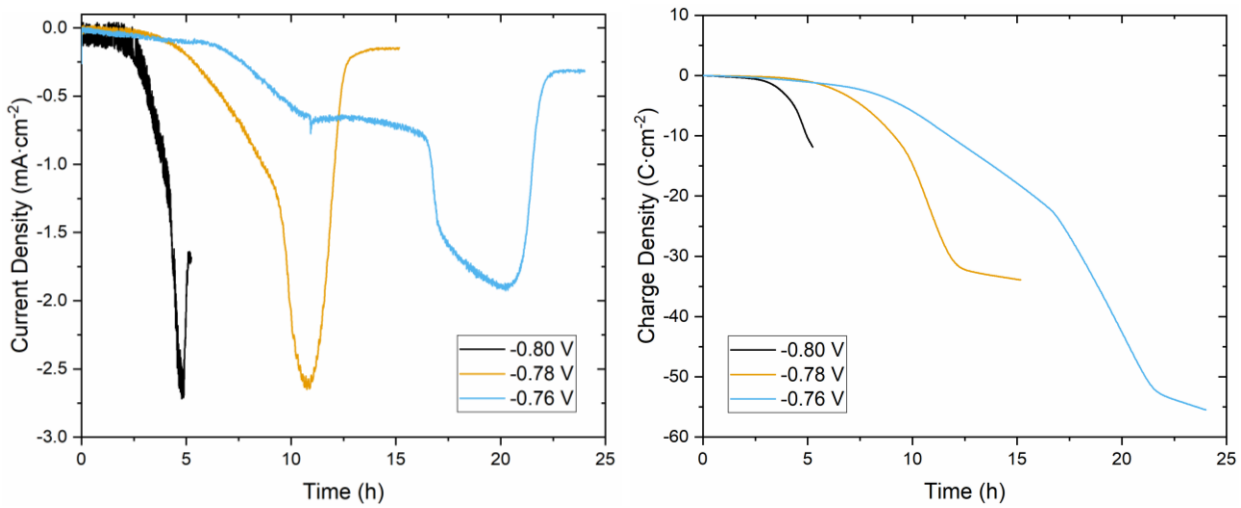

Figure 2: Transients of current density and charge density associated with Au electrodeposition at the indicated potentials on gratings with 94 μm deep 5.2 μm wide trenches at 8 μm pitch imaged in **Fig. 1**. Measured current and charge are converted using the projected, patterned areas of the substrates. Deposition inside the slot of the specimen holder masks the much slower Au nucleation and growth on the Pt seed during the first several hours at -0.76 V. Although not clear at the timescale of the plot, the transient at -0.80 V was terminated soon after the falling current began to rise once again with the emergence of active deposition from the trench openings onto the wider field. The deposition charge for fully dense Au fill is 53 $C \cdot cm^{-2}$ for a 100 % efficient process. Sources of experimental deviation from this value include inaccuracy in determination of specimen area, deposit voiding, irregular trench dimensions and deposition on the field. All three samples were rotating at 200 rpm with flow parallel to the field in 0.16 $mol \cdot L^{-1}$ $Na_3Au(SO_3)_2$ + 0.64 $mol \cdot L^{-1}$ Na_2SO_3 electrolyte of pH 9.0 containing 50 $\mu mol \cdot L^{-1}$ Bi^{3+}.

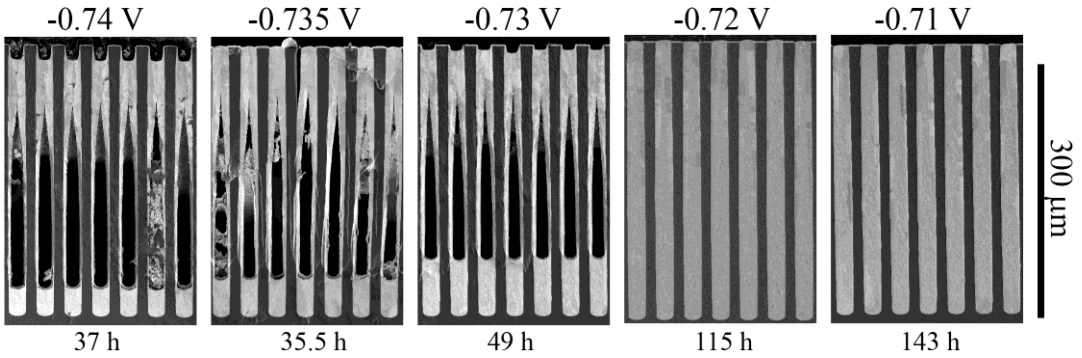

Figure 3: Scanning electron microscope images of Au electrodeposits in cross-sectioned gratings with 305 µm deep 21 µm wide trenches at 32 µm pitch. Deposition for the indicated times at the indicated filling potentials. In all cases filling was preceded by 13 h at -0.76 V followed by +5 mV steps, with a 2 h hold at each potential, to the filling potential, and activated deposition occurred only after the potential steps. All rotating at 100 rpm with the specimen suspended vertically in 0.16 mol·L^{-1} $Na_3Au(SO_3)_2$ + 0.64 mol·L^{-1} Na_2SO_3 electrolyte of pH 9.0 containing 50 µmol·L^{-1} Bi^{3+}.

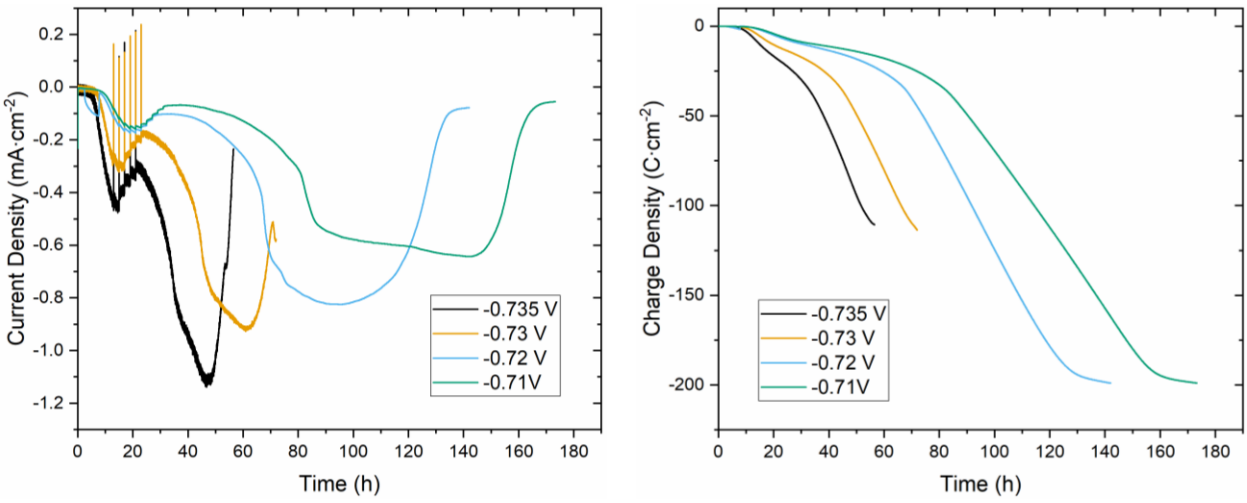

Figure 4: Transients of current density and charge density associated with Au electrodeposition at the indicated potentials on gratings with 305 µm deep 21 µm wide trenches at 32 µm pitch imaged in **Fig. 3** (data for deposition at -0.74 V was not collected). Filling for 35.5 h at -0.735 V,

49 h at -0.73 V, 115 h at -0.72 V and 143 h at -0.71 V was preceded by 13 h at -0.76 V and then +5 mV steps, with 2 h hold times, to the filling potential. Measured current and charge are converted using the planar projection of the patterned areas of the substrates. Relatively elevated current density during the first several hours at -0.72 V is associated with wetting of the holder; it does not contribute to the charge density significantly. The deposition charge for fully dense Au fill is ≈ 190 $C \cdot cm^{-2}$ for a 100 % efficient process. Sources of experimental deviation from this value include inaccuracy in determination of specimen area, deposit voiding, irregular trench dimensions and deposition on the field. All rotating at 100 rpm with the specimen suspended vertically in 0.16 $mol \cdot L^{-1}$ $Na_3Au(SO_3)_2$ + 0.64 $mol \cdot L^{-1}$ Na_2SO_3 electrolyte of pH in the range 9.0 to 8.8 containing 50 $\mu mol \cdot L^{-1}$ Bi^{3+}.

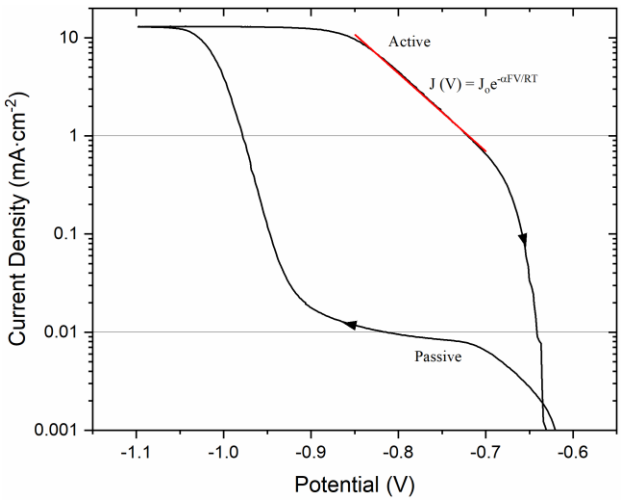

Figure 5: Cyclic voltammogram for 0.16 $mol \cdot L^{-1}$ $Na_3Au(SO_3)_2$ + 0.64 $mol \cdot L^{-1}$ Na_2SO_3 electrolyte of pH 9.0 containing 50 $\mu mol \cdot L^{-1}$ Bi^{3+} for a rotating disk electrode rotation rate of 100 rpm is shown using a logarithmic scale to capture the difference between the passive negative-going scan and the active positive-going scan over the range -0.85 V to -0.7 V. The linear fit of the active deposition rate on the return scan is overlaid. A 100× difference is indicated. The applied potential

was cycled from -0.6 V at 2 $mV \cdot s^{-1}$, and potentials are relative to SSE. Data was acquired using software compensation for 85 % of the measured 4 Ω cell resistance (i.e., < 1 Ω of uncompensated cell resistance). Current density is obtained from measured currents using the nominal area of the 1 cm diameter rotating disk electrode (RDE).

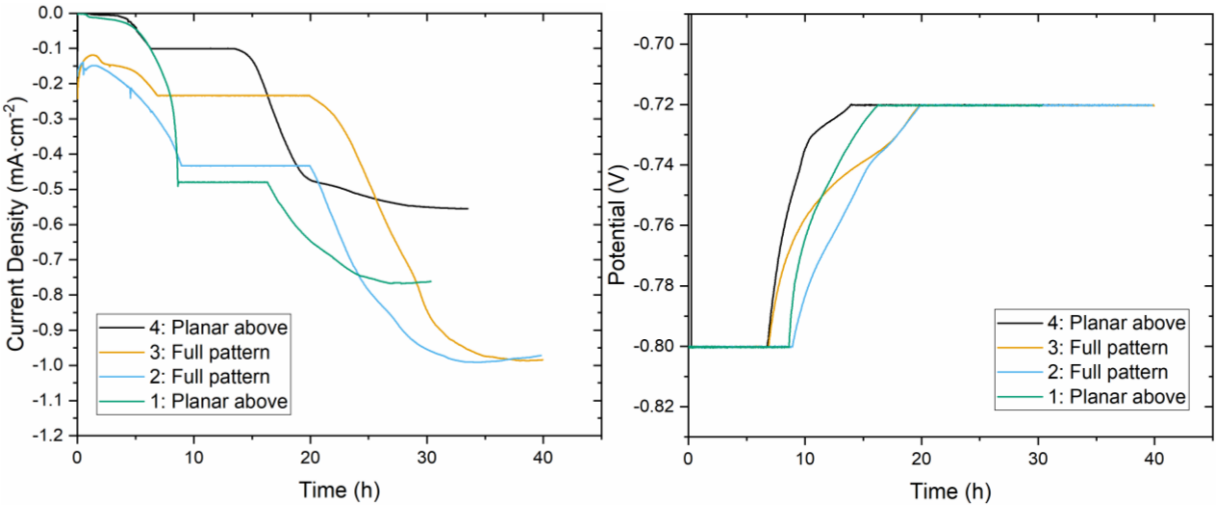

Figure 6: Transients of current density and potential associated with Au electrodeposition on gratings with 305 μm deep 21 μm wide trenches at 32 μm pitch using a combination of potentiostatic and potentiodynamic control processes. Measured current is converted to current density using the fully immersed areas of the patterned substrates. Capillary wicking of the electrolyte up the trenches toward the holder on specimens where the pattern extended above the electrolyte (Full pattern) increases the active area by only perhaps 20 % beyond the nominal value, but rapid nucleation and growth in this region underlies substantially more elevated initial current density. The contribution from passive deposition in the corresponding planar region of specimens where the patterned region was fully immersed (Planar above) is not significant. All rotating at

200 rpm with the specimen suspended vertically in 0.16 mol·L^{-1} $Na_3Au(SO_3)_2$ + 0.64 mol·L^{-1} Na_2SO_3 electrolyte of pH 9.0 containing 50 μmol·L^{-1} Bi^{3+}.

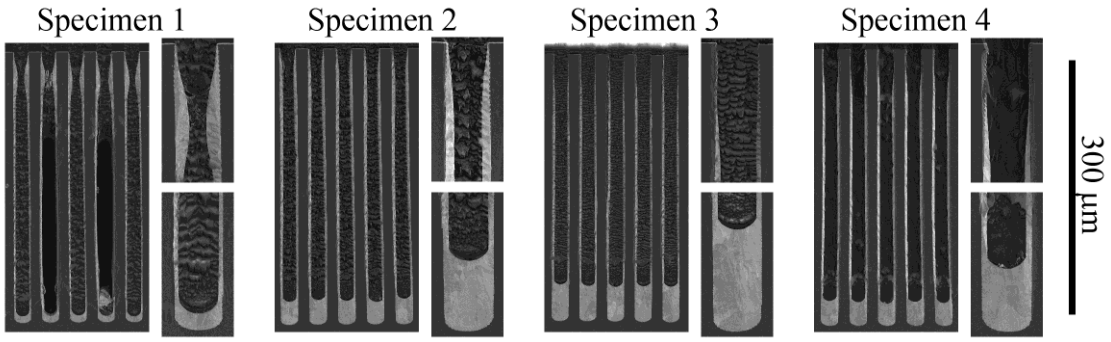

Figure 7: Fill in gratings having 305 μm deep 21 μm wide trenches at 32 μm pitch as a result of the deposition transients shown in **Fig. 6**. Inversion of deposit thickness on the sidewalls going down from the opening of the trench yields subconformal deposition, i.e., decreasing deposit thickness going deeper down the feature, in the upper region of Specimen 1. Modestly subconformal deposition is also evident upon comparison of the sidewall deposits in the upper and lower regions of Specimen 2. All rotating at 200 rpm with the specimen suspended vertically in 0.16 mol·L^{-1} $Na_3Au(SO_3)_2$ + 0.64 mol·L^{-1} Na_2SO_3 electrolyte of pH 9.0 containing 50 μmol·L^{-1} Bi^{3+}.

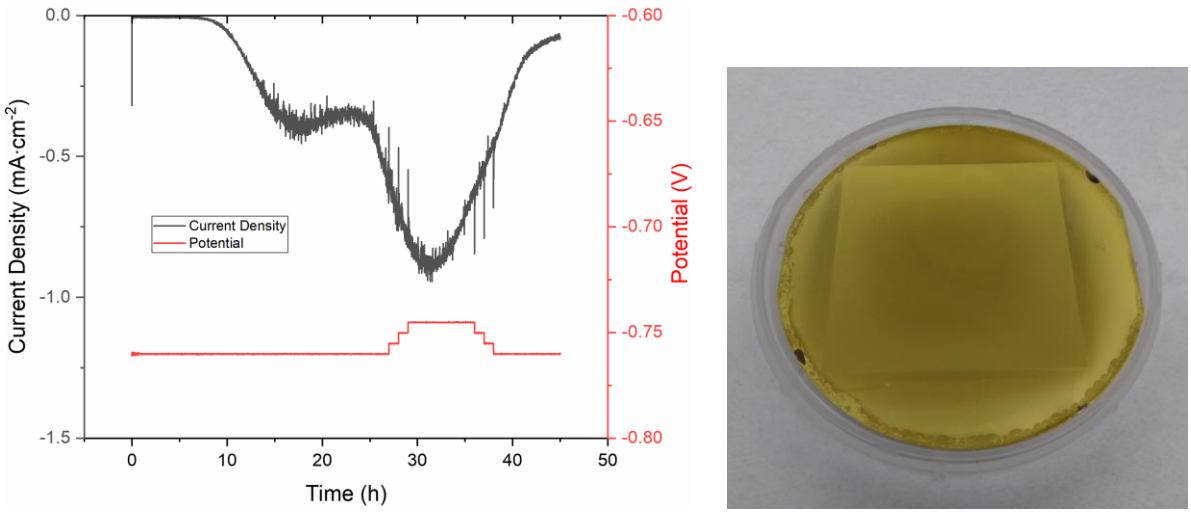

Figure 8: The current density and potential transients associated with fill of the pictured 65 mm square grating having 94 μm deep 5.2 μm wide trenches at 8 μm pitch patterned on a 100 mm Si wafer. Deposition while rotating at 200 rpm in 0.16 mol·L^{-1} $Na_3Au(SO_3)_2$ + 0.64 mol·L^{-1} Na_2SO_3 electrolyte of pH 9.0 containing 50 μmol·L^{-1} Bi^{3+}. The deposition charge of 54.6 C·cm^{-2} associated with the current transient modestly exceeds the 53 C·cm^{-2} value of a 100 % efficient process based on the pattern size and nominal trench width and depth. Sources of experimental deviation from this value include irregular trench dimensions and deposition on the field and rear of the wafer.

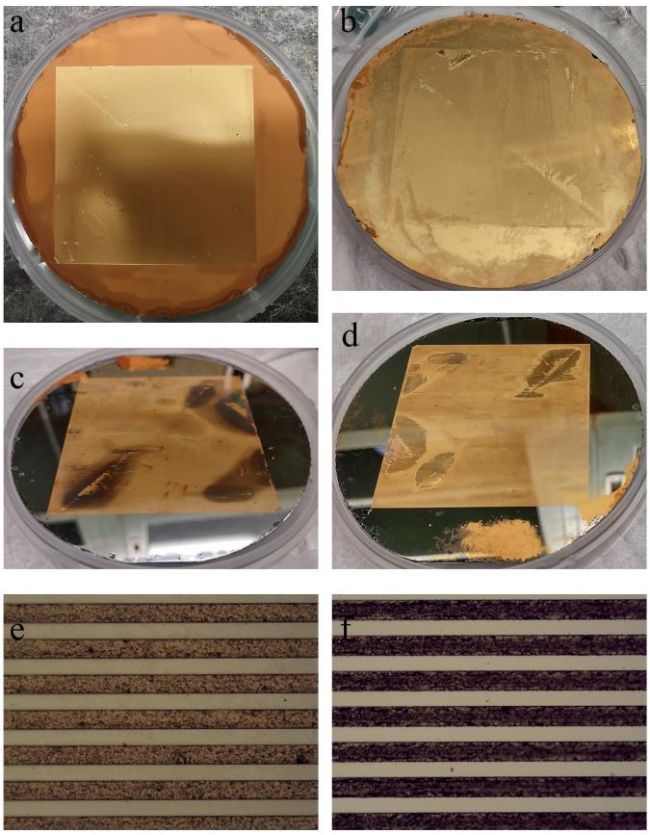

Figure 9: Images of a 100 mm Si wafer patterned with a 65 mm square grating having 305 μm deep 21 μm wide trenches at 32 μm pitch. a) The grating after fill to approximately 91 % of the trench height based on deposition charge. Small defects visible upon close examination result from perturbation of flow around fibers (i.e., dust) entrained in the trenches during processing. b) The wafer after a second bottom-up filling process. The use of overly aggressive conditions to rapidly reactivate bottom-up filling enabled deposition to extend above the openings of the trenches; macroscale surface deposits are evident inside the rear edge and along one diagonal of the pattern. c) The same wafer after removal of Au above the field through a blanket etch and localized etching of the overdeposits. The Au in the trenches surrounding the etched-back overdeposits is recessed several tens of micrometers from the field, giving these areas a Pt color. d) The wafer after a third bottom-up filling process and a short etch to remove Au from the Pt field for contrast. The previously recessed regions are a bright gold color from the freshly bottom-up filled deposits.

Higher magnification images show that the Au deposits are flush with the field where the deposits are e) bright after bottom-up filling in the third process and f) dark where the trenches remained filled after blanket etching that followed the second deposition process.

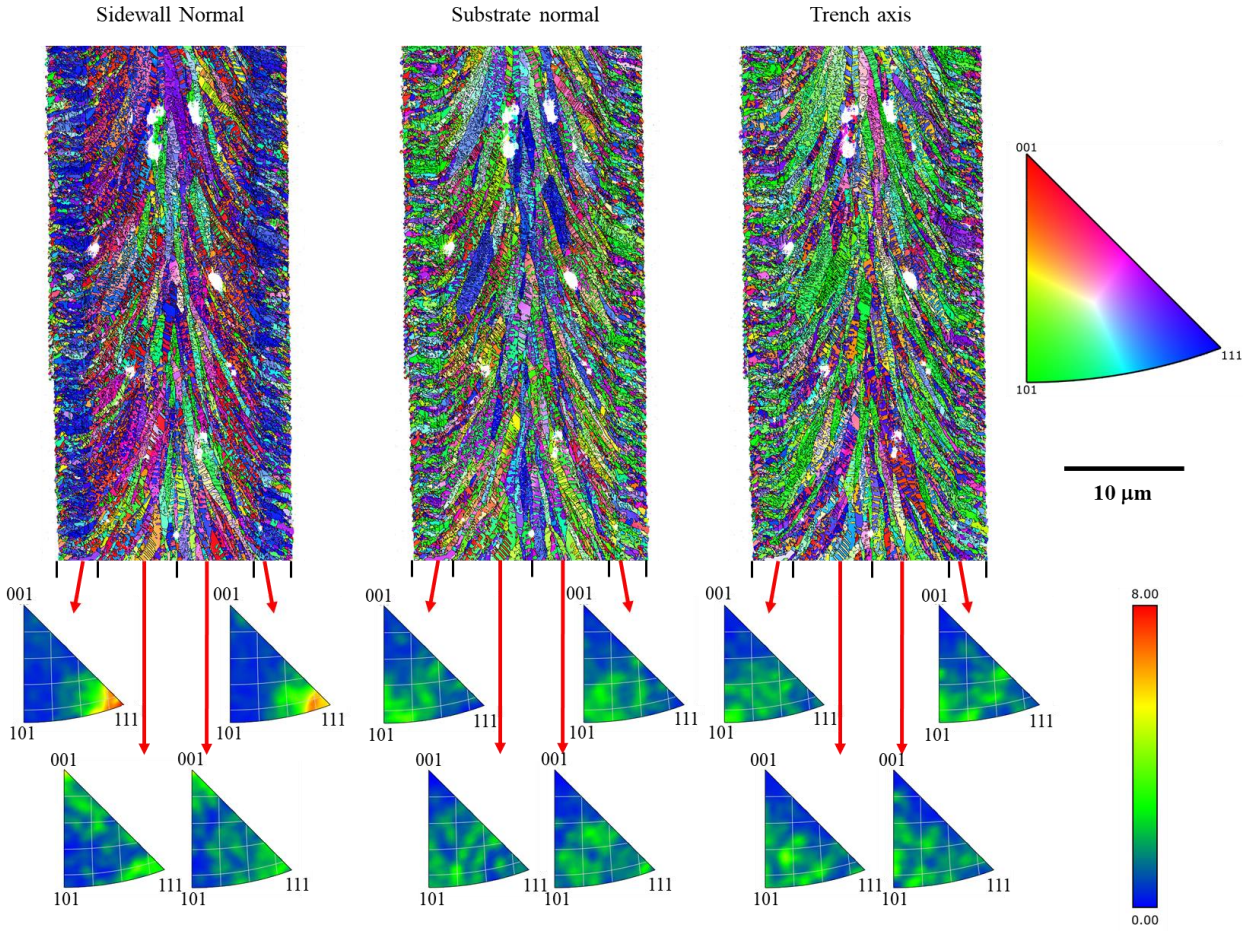

Fig. 10: EBSD maps showing the orientations of the Au grains in the lower portion of one trench in a cross-sectioned grating with 305 µm deep 21 µm wide trenches at 32 µm pitch. Grain orientations are shown in the directions normal to the plane of the substrate, normal to the sidewall and parallel to the trenches. The color triangle on the right shows the relationship between color in the map and crystal planes (hkl). Inverse pole figures (IPFs) capture the fraction of the deposit having a particular crystal orientation normalized by the fraction that would have the orientation

in a random distribution; the four IPFs beneath each map are for the indicated regions adjacent to the sidewalls and the left and right halves of the central deposit. The intensity color scale bar for the IPFs is shown on the right. White spots, indicating failure to assign grain orientation, are from carbonaceous deposits on the catalytic surface due to storage. Filling for 13 h at -0.72 V was preceded by 13 h at -0.76 V followed by +5 mV steps, with a 2 h hold at each potential, to the filling potential of -0.72 V, at which potential deposition continued for 115 h. Rotating at 100 rpm with the specimen suspended vertically in 0.16 $mol \cdot L^{-1}$ $Na_3Au(SO_3)_2$ + 0.64 $mol \cdot L^{-1}$ Na_2SO_3 electrolyte of pH 9.0 containing 50 $\mu mol \cdot L^{-1}$ Bi^{3+}.

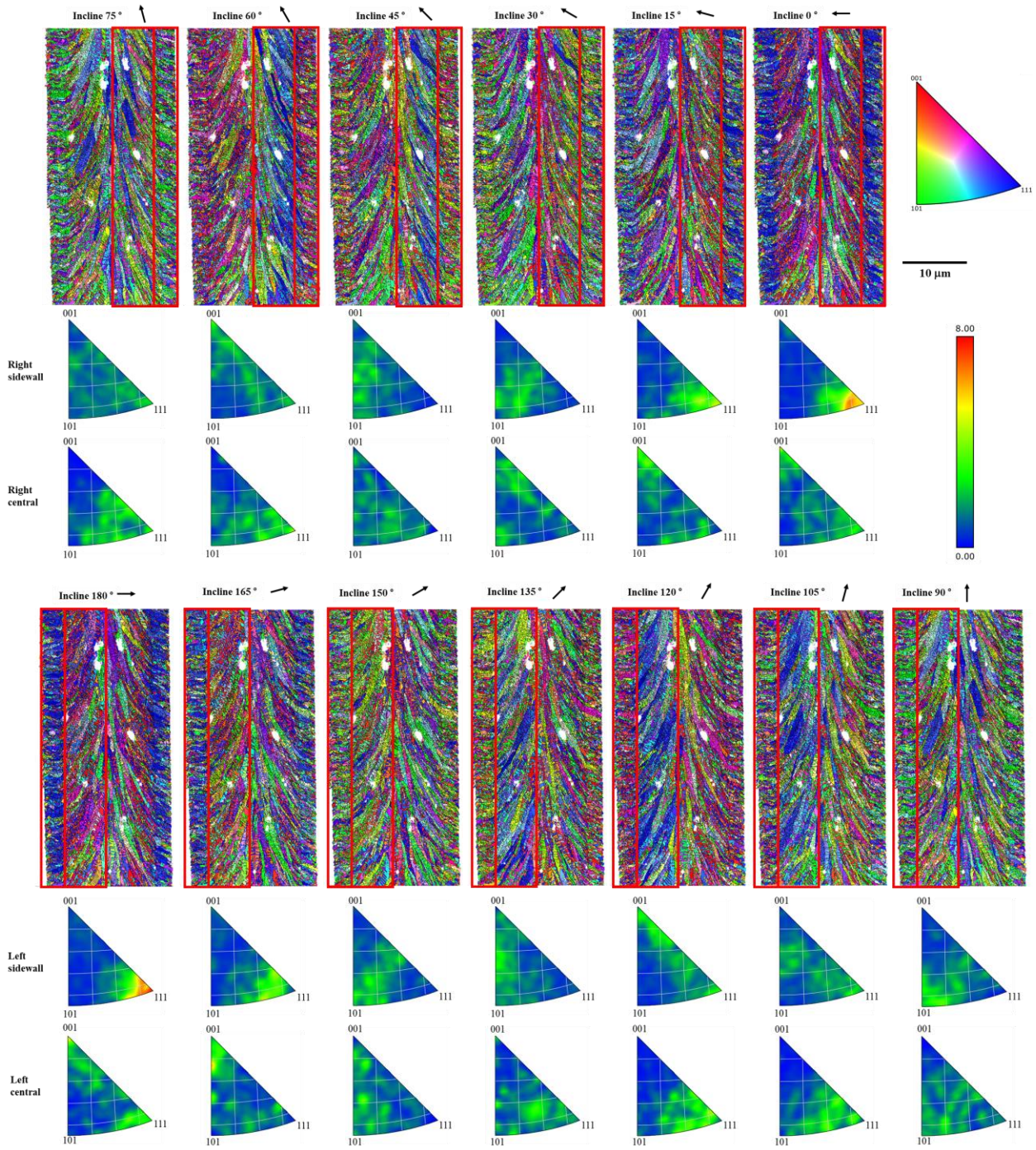

Fig. 11: EBSD maps showing the orientations of the Au grains in the lower portion of one trench in a cross-sectioned grating with 305 µm deep 21 µm wide trenches at 32 µm pitch. Grain orientations are relative to the direction indicated by the arrow above each map. The color triangle on the right shows the relationship between color in the map and crystal planes (hkl). Inverse pole

figures (IPFs) capture the fraction of the deposit having a particular crystal orientation normalized by the fraction that would have the orientation in a random distribution; two IPFs beneath each map indicate distributions in the region adjacent to the sidewalls and the central portion in either the left or right half of the trench, as indicated, with the scale bar shown on the right. Filling for 13 h at -0.72 V was preceded by 13 h at -0.76 V followed by +5 mV steps, with a 2 h hold at each potential, to the filling potential of -0.72 V, at which potential deposition continued for 115 h. Rotating at 100 rpm with the specimen suspended vertically in 0.16 $mol \cdot L^{-1}$ $Na_3Au(SO_3)_2$ + 0.64 $mol \cdot L^{-1}$ Na_2SO_3 electrolyte of pH 9.0 containing 50 $\mu mol \cdot L^{-1}$ Bi^{3+}.

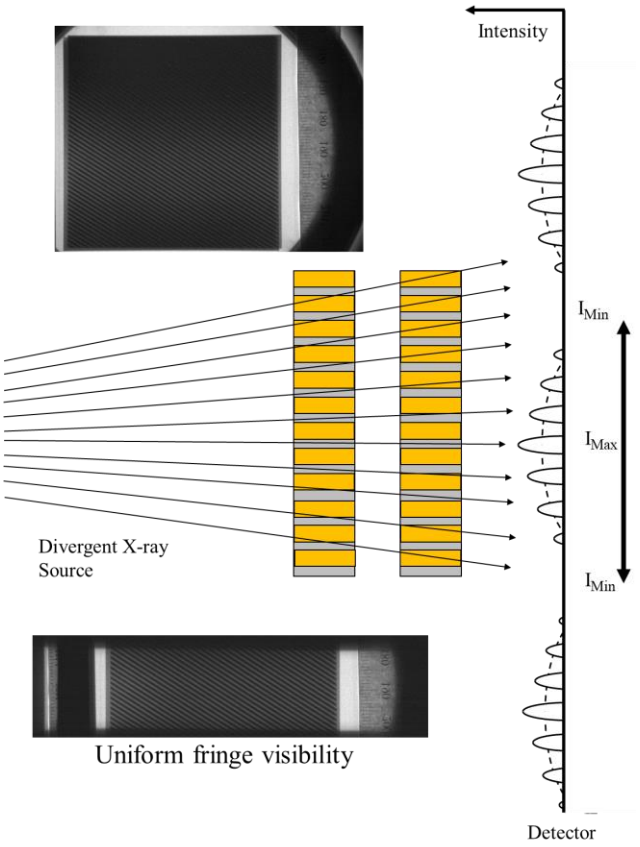

Figure 12: Moiré patterns in the X-ray intensity obtained on the screen of the detector using two gratings with bottom-up Au filled 94 μm deep 5.2 μm wide trenches at 8 μm pitch. A schematic of the experimental geometry that captures the origin of the Moiré fringes is shown as well. The transmitted intensity exhibits oscillations at a micrometer scale defined by the pitch of the trenches on the gratings such as is indicated by the solid curves. Due to the very different X-ray attenuation in Si and Au at the X-ray energies used the maxima and minima of these oscillations differ by orders of magnitude. The divergence of the X-ray source, increased here for clarity, coupled with the spacing between the two gratings underlies the beating of the pattern. The optical measurement system resolves the locally averaged intensity of the Moiré fringes indicated by the dashed curve.

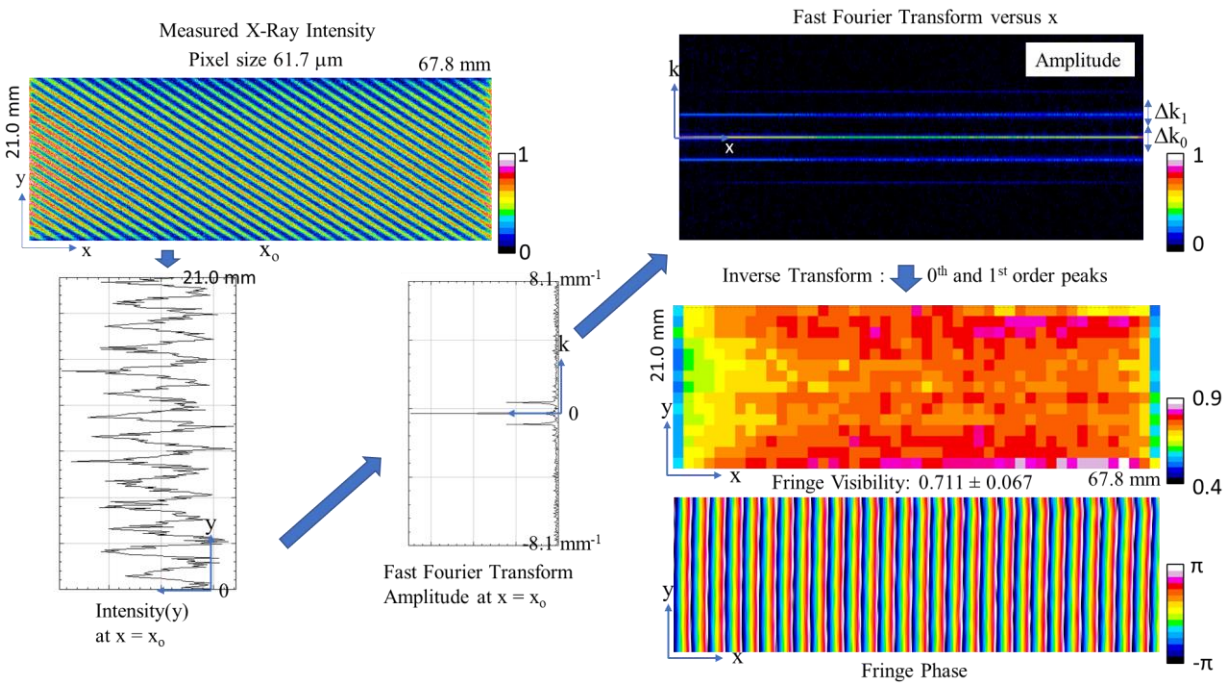

Figure 13: The sequence from X-ray transmission mapping through visibility assessment is captured. First is the Moiré fringe pattern obtained from two bottom-up Au filled gratings having 94 μm deep 5.2 μm wide trenches at 8 μm pitch illuminated by an X-ray source at 40 kV with transmitted X-ray intensity measured on the detector screen at resolution defined pixel spacing of 61.7 μm in both *x* and *y*. Next, the oscillating intensity in the y-direction is shown at position x_o. The amplitude of the Fast Fourier Transform of this oscillating intensity, shown thereafter, captures a strong 0^{th} order central peak and strong (identical) ± 1^{st} order peaks. This is followed by a map of the amplitude of the transform of the fringe pattern versus position along *x*. The inverse transform is evaluated over wavenumbers in the ranges Δk_0 and Δk_1 to obtain the spatial distribution of the 0^{th} and 1^{st} order components. Visibility and phase values are obtained at *y* locations spaced by 1.4 mm, finer resolution providing no additional information given the *k*-value of the peak, at the 61.7 μm pixel resolution of the original fringe pattern in *x*. The visibility values

were averaged over 1.4 mm intervals of *x* to obtain an approximately square pixilation in the fringe visibility map. The average value and standard deviation of the associated values are indicated.

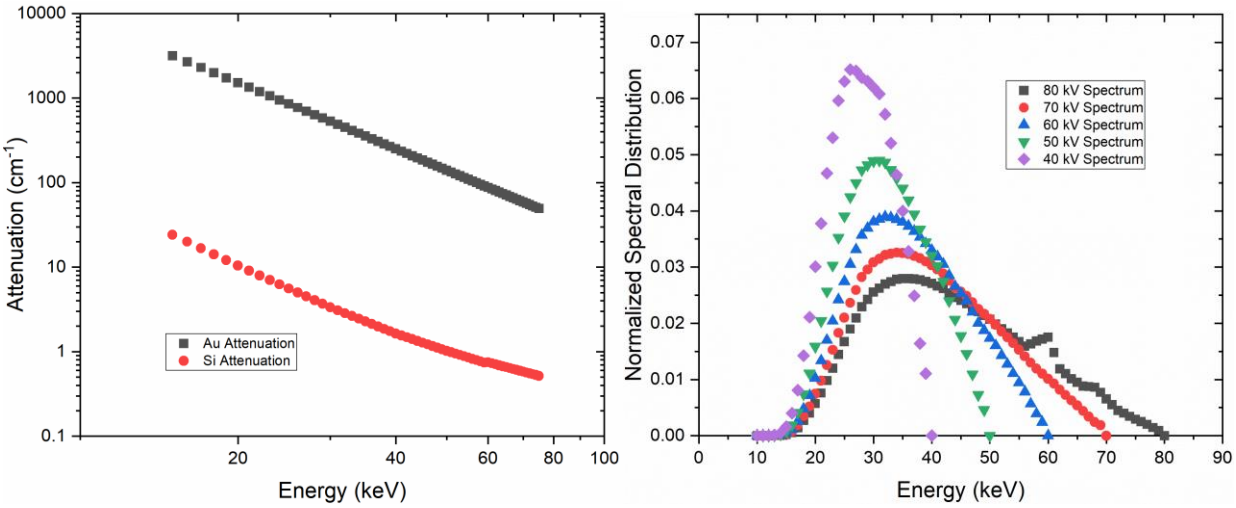

Figure 14: a) X-ray attenuation coefficients for fully dense Au (19.32 g·cm^{-3}) and Si (2.33 g·cm^{-3}). Values for each material at 10 keV, 15 keV, 20 keV, 30 keV, 40 keV, 50 keV, 60 keV and 80 keV are from NIST's database[43]; the remaining values, at 1 kV intervals, are interpolated assuming log-linear (i.e., power dependent) behavior in each interval. b) Normalized distributions of X-rays from a tungsten X-ray tube plotted as a function of X-ray energy for the indicated tube voltages.[44]

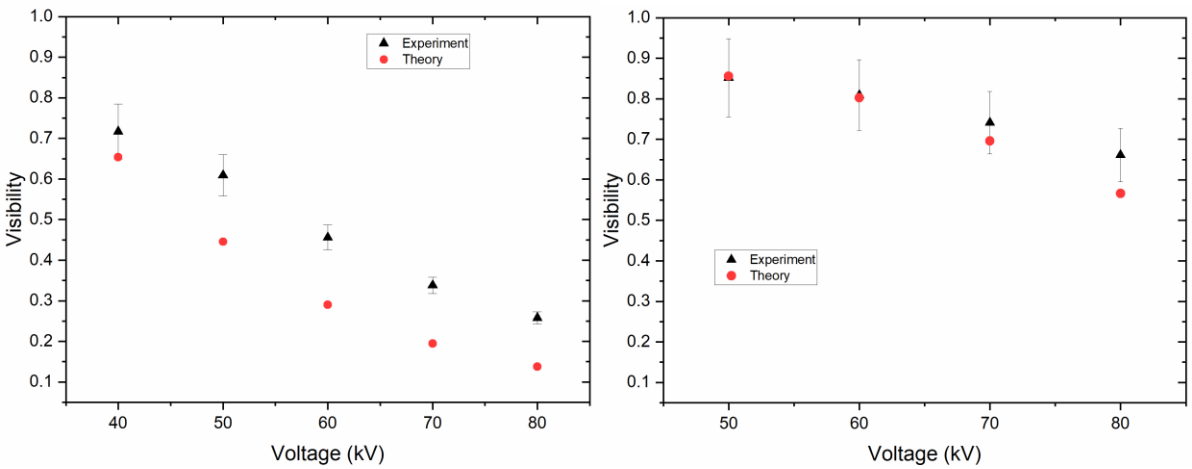

Figure 15: The average visibilities of pairs of bottom-up Au filled gratings with a) 94 μm deep 5.2 μm wide trenches at 8 μm pitch and b) 305 μm deep 21 μm wide trenches at 32 μm pitch are compared to predicted values as a function of the X-ray tube voltage. Experimental values were assessed using a tungsten slit to select the central third of the 65 mm × 65 mm gratings, removing regions at the edges of the patterns with lower fringe visibility caused by increasing misalignment of the tall trenches in the planar gratings from the divergent X-ray source farther from the midline. Fringe visibility values are as measured from the intensity maps. Predicted values model transmission through dense Au that fully fills the trenches patterned in the Si wafers at a 65:35 ratio of Au:Si area in both sets of trench arrays. The values are obtained using the X-ray spectra and energy-dependent attenuation curves in **Fig. 14**, accounting for transmission through the unetched backplanes of the 0.5 mm thick Si wafers into which the gratings are patterned, with Fourier analysis providing the spectral distribution of X-ray intensity transmitted across the area of the detector. Light leakage across the phosphor screen used in the detector is accounted for, but transmission of high energy X-rays through the phosphor screen without absorption is not.